Nuclear RNAi Modulates Influenza A Virus Infectivity By Downregulating Type-I Interferon Response

Hsiang-Chi Huang[1,2,3,#], Vivian Lobo[1, 2], Karin Schön[3], Iwona Nowak[1, 2], Jakub O. Westholm[4], Carola Fernandez[1,2], Angana A.H. Patel[2,5], Clotilde Wiel[5], Volkan I. Sayin[2,5], Dimitrios G. Anastasakis[6], Davide Angeletti[3,7§,#] and Aishe A. Sarshad[1,2,8,§,#]

1 Department of Medical Biochemistry and Cell Biology, Institute of Biomedicine, University of Gothenburg, SE-40530 Gothenburg, Sweden

2 Wallenberg Centre for Molecular and Translational Medicine, University of Gothenburg, SE-40530 Gothenburg, Sweden

3 Department of Microbiology and Immunology, Institute of Biomedicine, University of Gothenburg, SE-40530 Gothenburg, Sweden

4 Dept of Biochemistry and Biophysics, National Bioinformatics Infrastructure Sweden, Science for Life Laboratory, Stockholm University, Box 1031, SE-17121 Solna, Sweden

5 Department of Surgery, Institute of Clinical Sciences, Sahlgrenska Center for Cancer Research, University of Gothenburg, SE-40530 Gothenburg, Sweden

6 RNA Molecular Biology Laboratory, National Institute for Arthritis and Musculoskeletal and Skin Disease, Bethesda, MD 20892, USA.

7 SciLifeLab, University of Gothenburg, SE-40530 Gothenburg, Sweden

8 Lead contact

[§] Joint senior authors

[#] Correspondence to hsiang-chi.huang@gu.se, davide.angeletti@gu.se, aishe.sarshad@gu.se

Keywords: Argonaute 2; influenza A virus; p53; nuclear RNAi; type-I interferons; fPAR-CLIP; TRIM71

ABSTRACT

The role of Argonaute (AGO) proteins and the RNA interference (RNAi) machinery in mammalian antiviral response has been debated. Therefore, we set out to investigate how mammalian RNAi impacts influenza A virus (IAV) infection. We demonstrate that IAV infection triggers nuclear accumulation of AGO2, which is directly facilitated by p53 activation. Mechanistically, we show that IAV induces nuclear AGO2 targeting of TRIM71, a proposed AGO2 E3 ligase, and type-I interferon-pathway genes for silencing. Hence, the RNAi machinery is highjacked by the virus to evade the immune system and support viral replication. We demonstrate that the FDA approved drug arsenic trioxide prevents nuclear AGO2:p53 accumulation, thereby increasing interferon response and decreasing viral replication *in vitro* and in a mouse model *in vivo*. Our data indicates that targeting the AGO2:p53-mediated silencing of innate immunity may offer a promising strategy to mitigate viral infections.

INTRODUCTION

Argonaute (AGO) proteins have a central role in RNA interference (RNAi), where they are guided by endogenous miRNA or exogenous siRNA to recognize (partially) complementary sequences on target RNAs [1]. Together, AGO-small RNA (smRNA) constitutes the core of the RNA-induced silencing complex (RISC), a multiprotein complex that deregulates RNA transcripts, resulting in target destabilization [1]. RNAi has a well-established role in antiviral defense in certain eukaryotes, including plants, insects and nematodes [2,3]. However, in mammals, the role of RNAi as an antiviral defense mechanism is more controversial: indeed, while some studies described antiviral RNAi functions [4,5], many others reported a lack of evidence for direct antiviral activity [6]. What has not been extensively investigated is whether RNAi could be hijacked by viruses to their advantage. Sparse evidence suggests that loss of RNAi after viral infection may indeed decrease viral titers with concomitant increased expression of antiviral genes [6-8]. The overall picture and detailed mechanisms of action remain, however, elusive.

Upon infection with influenza A virus (IAV), the innate immune system serves as the body's primary defense, swiftly initiating a response to combat invading pathogens [9]. A crucial facet of the innate immune response to IAV is the synthesis of type-I interferons (IFN-Is) by infected cells. These interferons subsequently activate neighboring cells to produce antiviral proteins, which are essential in curtailing the severity and duration of infections [10]. Viral RNAs, in their single-strand or intermediate format, can be recognized by the Toll-like receptors TLR3 and TLR7 to activate IFN transcription via NF-kβ, IRF-3 or IRF-7 [9]. Collectively, viral RNAs therefore activate the immune system by different mechanisms, which all lead to interferon production. Additionally, the tripartite motif (TRIM) family of proteins modulates the production, signaling, and effector functions of IFN-Is, thereby influencing immune responses and host defense against pathogens. Notably, TRIM25, TRIM56, and TRIM71 exert positive regulatory roles in the IFN-I pathway [11].

From the IAV side, the multifunctional nonstructural protein 1 (NS1) of IAV serves as an RNA-binding protein, facilitating mRNA export from the nucleus. Interestingly, NS1 can re-enter the cell nucleus and has a pivotal role in antagonizing host immune responses and facilitating pathogenesis [12-15]. Furthermore, NS1 has been shown to inhibit TRIM25 oligomerization, thus suppressing RIG-I-mediated IFN production [16]. Therefore, NS1 is the key player in IAV innate immune evasion, with multiple functions; notably, NS1 is also able to block RISC ribosylation [7]. It has been shown that ribosylation of the RISC complex leads to

77 the shutdown of RNAi mechanisms. This is intriguing because it suggests that it is in the virus'
78 best interest to maintain RNAi function. However, while it was shown that two specific
79 miRNAs could inhibit interferon-stimulated genes (ISGs) in IFN-treated cells, there are still
80 open questions regarding global, mechanistic functions of RNAi after viral infections.
81 Adding to the complexity of viral regulation of RISC function is the identification of
82 nuclear RNAi. In metazoans, cytoplasmic RNAi processes are well documented [17], yet the core
83 RISC components – AGOs and miRNAs – have been found in cell nuclei [18-21]. Indeed, various
84 mechanisms of stress-induced nuclear translocation of AGOs have been proposed, including
85 DNA damage and viral infection [22,23]. While cytoplasmic AGO2 is well known as a critical
86 component of RISC and is involved in siRNA/miRNA-mediated gene suppression pathways
87 [24], little is known about the specific functions of nuclear AGO2. This is particularly relevant to
88 disentangle the controversies around the role of RNAi in mammals after viral infections.
89 To comprehensively address the role of RNAi following IAV infection, we combined
90 *in vitro* and *in vivo* experimental models with fluorescence-based photoactivatable
91 ribonucleoside-enhanced crosslinking and immunoprecipitation (fPAR-CLIP) to pinpoint
92 AGO2 targets at nucleotide resolution. We demonstrate that upon IAV infection, NS1 mediates
93 AGO2 translocation into the cell nucleus to silence TRIM71 and IFN-pathway-related genes,
94 thereby increasing viral replication. Our data provide important mechanistic insights into
95 previously underappreciated modalities of viral resistance.
96

97 **RESULTS**

98 **Viral infection induces nuclear accumulation of AGO2**

99 AGO2 may localize both in the cytoplasm and the nucleus of human cells [25]. For instance, we
100 previously demonstrated the absence of nuclear AGO2 in HEK293 cells [21,25] However, we
101 observed a high degree of nuclear AGO2 in HEK293T cells, which are HEK293 cells
102 transformed with SV40 large T (LT) antigen, the master regulator of polyomaviruses [26] (**Fig**
103 **1A**). Biochemical fractionation of HEK293T cells showed a near 50-50 distribution of AGO2
104 between the cytoplasmic and nuclear fractions (**Fig 1A**). Moreover, transient overexpression
105 of SV40 LT antigen in HEK293 cells led to the translocation of AGO2 into the nucleus (**Fig**
106 **1B**), indicating the involvement of SV40 LT antigen in AGO2 nuclear accumulation. These
107 observations prompted us to investigate whether nuclear translocation of AGO2 is a general
108 feature of viral infections.

109 To address this, we took advantage of PR8 strain of IAV as a model system. HEK293
110 cells were infected with PR8-IAV at several multiplicity of infection (MOI) 10 for 16 hours,
111 and biochemical fractionation experiments were performed (**Fig 1C**). Remarkably, we
112 observed robust nuclear translocation of AGO2 upon infection with PR8-IAV (**Fig 1C**).
113 Intriguingly, we also observed the nuclear translocation of AGO1, AGO3, and AGO4 proteins
114 at MOI of 10 (**Fig 1C**), suggesting that the nuclear accumulation of RNAi factors is a general
115 phenomenon during IAV infection. To visualize the nuclear accumulation of AGO2 upon viral
116 infection, we utilized a fluorescently tagged PR8 virus strain, which has mCherry inserted
117 within the NS1 protein [27], and performed confocal microscopy (**Fig 1D**).

118 IAV consists of eight gene segments that encode up to 17 viral proteins [28]. To identify
119 the specific gene segment responsible for AGO2 nuclear accumulation, we transiently
120 expressed each influenza protein in HEK293 cells and performed biochemical fractionation
121 assays. Interestingly, we found that NS1 is the primary viral factor triggering AGO2 nuclear
122 translocation (**Fig 1E**). Furthermore, we observed nuclear co-localization of AGO2 with NS1
123 after transient expression of mCherry-tagged NS1 protein (**Fig 1F**). Collectively, these findings
124 suggest that viral proteins, including SV40 LT antigen and IAV NS1, induce nuclear
125 accumulation of AGO1-4.

126

127 **AGO2 interacts with p53 in the nucleus upon viral infection**

128 Having established the nuclear translocation of AGO2, after IAV infection, we next wanted to
129 identify potential interacting partners of AGO2 involved in its translocation or stabilization.
130 Therefore, we retrieved a list of AGO2-associated proteins (**Sup Table 1**) from the

131 Harmonizome database [29], and performed a protein-protein interaction network analysis by
132 STRING (**Fig 2A**). We identified that AGO2 directly interacts with p53, as well as with other
133 well-known components of the RISC complex (**Fig 2A**). Interestingly, SV40 LT antigen also
134 possesses a p53 binding domain [30], Therefore, we wondered whether p53 may play a role in
135 the nuclear translocation of AGO2 after viral infection and whether p53 can also interact with
136 the NS1 component of IAV.
137 To address these questions, we first examined the subcellular localization of p53 in
138 HEK293 cells. We observed that p53 levels are low, yet ubiquitous, in HEK293 cells but, as
139 reported, the majority of p53 translocated into the nucleus when cells are treated with
140 doxorubicin, a DNA damage-inducing agent, for 24 hours (**Fig 2B**) [31]. Consistent with our
141 hypothesis, AGO2 also translocated into the nucleus in doxorubicin -treated cells (**Fig 2B**).
142 Further, by performing a co-immunoprecipitation experiment, we demonstrated a direct
143 interaction between AGO2 and p53 upon doxorubicin treatment (**Fig 2C**). Interestingly, in
144 HEK293T (**Sup Fig 1A**), neuroblastomas cells SK-N-BE(2) (**Sup Fig 1B**) and breast cancer
145 cell line MCF7 (**Sup Fig 1C**) AGO2 and p53 are ubiquitously expressed but interact
146 exclusively within the nucleus (**Sup Fig 1A-C**).
147 Next, we investigated the subcellular localization of p53 in response to transient
148 expression of SV40 LT antigen (**Fig 2D**) and NS1 (**Fig 2E**). Indeed, overexpression of both
149 viral proteins induced substantial translocation of p53 into the nucleus, together with AGO2
150 (**Fig 2D,E**). Furthermore, in IAV-infected HEK293 cells, we observed not only nuclear AGO2
151 but also nuclear p53 accumulation (**Fig 2F**). Finally, to test whether AGO2 and p53 interact
152 with each other also in response to viral infection, we co-immunoprecipitated AGO2 with p53.
153 Indeed, we observed an interaction between AGO2 and p53 in virus-infected cells but not in
154 control cells (**Fig 2G**). Similarly, we found that the p53:AGO2 co-immunoprecipitated after
155 transient expression of either SV40 LT (**Fig 2H**) or NS1 antigen (**Fig 2I**).
156 Taken together, our findings suggest that both AGO2 and p53 translocate into the
157 nucleus where they interact with each other in response to IAV infection. Furthermore, in cells
158 which already have nuclear AGO2, p53 and AGO2 interact, indicating a potential functional
159 interplay between these two proteins in the nucleus.
160
161 **The N-terminus of tetrameric p53 interacts with AGO2 and protects AGO2 from**
162 **proteasomal degradation in the nucleus.**
163 We next wanted to examine how AGO2:p53 interact and what functional outcome the
164 interaction may have in the nucleus. p53 is a 53 kDa protein consisting of an N-terminal

165 transactivation domain, proline-rich domain, a core DNA binding domain and a C-terminal
166 tetramerization and regulatory domain [32] (**Fig 3A**). The PIWI domain of AGO2 contains
167 tandem tryptophan-binding pockets, which collectively form a region for interacting with
168 TNRC6 or other tryptophan-rich cofactors [33,34]. Interestingly, we observed the presence of three
169 tryptophan residues (Trp23, Trp53, and Trp91) within the flexible N-terminal loop region of
170 p53 (**Sup Fig 2A**), suggesting that the N-terminus may be involved in AGO2 binding. To
171 investigate the possible interaction between the N-terminal region of p53 and AGO2, we
172 generated two flag-p53 mutants by removing amino acids 1-61 (Δ61 mutant) and 1-91 (Δ91
173 mutant) from the N-terminus (**Fig 3B**). Upon transient overexpression of these mutants in
174 doxorubicin-treated HEK293 cells, we found that AGO2 exclusively interacts with full-length
175 flag-p53, while the interaction was abolished in both N-terminal mutants (**Fig 3C**).
176 Activated p53 tetramerizes in the nucleus [35] and therefore we next wanted to test if the
177 tetrameric form is essential to interact with AGO2. In SK-N-BE(2) cells, known to possess
178 intact TP53 transcriptional activity, AGO2:p53 interacts in the nucleus (**Sup Fig 1B**) [36]. To
179 explore the effect of p53 monomerization, we treated SK-N-BE(2) cells with increasing
180 concentrations of arsenic trioxide (ATO), a known inducer of p53 monomerization, for 24
181 hours [37]. Remarkably, we observed a significant reduction in nuclear p53 localization with 0.1
182 μg/ml ATO treatment, and complete displacement of nuclear p53 at 0.5 μg/ml (**Sup Fig 2B**).
183 Strikingly, AGO2 was also displaced from the nucleus upon treatment with 0.5 μg/ml ATO
184 (**Sup Fig 2B**). Similar results were observed in HEK293T (**Fig 3D**) and MCF7 (**Fig 3E**) cells,
185 where nuclear AGO2 and p53 accumulate in the cytoplasm after ATO treatment. Being able to
186 manipulate p53 into its monomeric state, we next examined whether AGO2:p53 can interact
187 under these conditions. Consequently, we performed co-immunoprecipitation assays in the
188 above-mentioned cell lines, using whole cell lysates, in the presence or absence of ATO, and
189 found that ATO-mediated monomerization of p53 reduces its capability to interact with AGO2
190 (**Fig 3F,G**), highly suggestive of the fact that p53 and AGO2 only interact in the nucleus.
191 Having found a robust interaction between AGO2:p53, we next wanted to gauge for its
192 biological significance. To test whether p53 plays a role in the stability of AGO2, we silenced
193 *TP53* using siRNAs. *TP53* silencing resulted in a decrease in AGO2 protein levels in MCF7
194 and HEK293T cells (**Fig 3H,I**), suggesting that p53 may indeed stabilize AGO2 in the nucleus.
195 However, silencing AGO2 in the same cells did not lead to reciprocal instability of p53 (**Fig**
196 **3H,I**) further corroborating the specificity of p53 mediated stability of AGO2. To confirm these
197 findings, we employed p53 low-expressing MCF7 cells (hereafter referred to as TP53L cells).

198 Biochemical fractionation assays in wildtype (WT) and TP53L MCF7 cells revealed a similar
199 downregulation of AGO2 protein levels, specifically in the nucleus, upon loss of p53 (**Fig 3J**).
200 So far, we demonstrated that tetrameric p53 is needed for an interaction with AGO2 in
201 the nucleus, however, it remained unclear whether p53 is needed for nuclear import of AGO2
202 or to stabilize AGO2 within the nucleus. Therefore, we tested if AGO2 is degraded by the
203 ubiquitin-proteasome system when p53 is monomeric, by combining ATO treatment with the
204 proteasome inhibitor MG132. In cells treated with MG132 and ATO, we found that AGO2 co-
205 immunoprecipitated with anti-ubiquitin antibodies, indicating that AGO2 is tagged with
206 ubiquitin for proteasome degradation in the absence of nuclear p53 (**Fig 3K**).
207 Collectively, our findings demonstrate an interaction between p53 and AGO2 in the
208 nucleus, mediated by tetrameric p53. The interaction with p53 stabilizes AGO2 and protects it
209 from proteasomal degradation.
210
211 **Nuclear AGO2 facilitates viral infection**
212 Having observed that there is a significant influx of both AGO2 and p53 into the nucleus upon
213 viral infection and that p53 stabilizes AGO2 in the nucleus, we next aimed at determining if
214 and how this phenomenon would influence viral infection. Specifically, we addressed whether
215 nuclear AGO2:p53 serves as a proviral or an antiviral mechanism. To confirm whether the lack
216 of p53 inhibits AGO2 translocation to the nucleus upon viral infection, we conducted
217 biochemical fractionation experiments in WT and TP53L MCF7 cells, with or without viral
218 infection, and found that AGO2 was predominantly localized in the nucleus of WT MCF7 cells,
219 regardless of viral infection dose (**Fig 4A**). In contrast, AGO2 remained cytoplasmic in TP53L
220 MCF7 cells, irrespective of viral infection load (**Fig 4B**). Furthermore, we measured viral gene
221 expression in WT and TP53L MCF7 cells and observed a significant reduction of NS1 and HA
222 mRNA levels in p53-low cells (**Fig 4C**). Similarly, we also employed siRNA-mediated
223 silencing of *TP53* in HEK293 cells followed by IAV infection and quantified the levels of viral
224 mRNA. We observed a similar decrease in viral NS1 and HA gene expression upon IAV
225 infection in p53-silenced cells (**Fig 4D, Sup Fig 3A**). To further verify that RNA expression
226 of viral genes was correlated with viral infectivity, we infected WT and TP53L MCF7 cells
227 with PR8-mCherry virus and measured mCherry expression in infected cells using flow
228 cytometry. Indeed, only WT, but not TP53L MCF7 cells, successfully supported viral
229 replication (**Fig 4E**). Overall, the reduced mRNA expression of NS1 and HA observed upon
230 viral infection correlated with the lack of AGO2:p53 nuclear translocation (**Fig 4A-C**). Finally,
231 we investigated the reversibility of this phenomenon by overexpressing p53 in TP53L MCF7

232 cells. Remarkably, p53 overexpression not only restored viral gene expression (**Fig 4F)** but
233 also promoted AGO2 nuclear accumulation (**Fig 4G**). Our data indicated that IAV infection is
234 facilitated through the nuclear localization of AGO2:p53 complexes, however, it could not
235 distinguish between a key role of either nuclear AGO2 or p53 in mediating the proviral
236 outcome. Therefore, to test if AGO2 is essential in facilitating viral infectivity, we silenced
237 *AGO2* in HEK293 cells by siRNAs, infected the cells with IAV and finally measured the
238 mRNA levels of viral genes by qRT-PCR. It is important to consider that silencing *AGO2* did
239 not affect the stability of nuclear p53 (**Fig 3H-I**). We found that mRNA levels of viral genes
240 decreased when AGO2 was silenced (**Fig 4H, Sup Fig 3B)**. The mRNA levels of viral genes
241 was similar in siAGO2 *vs* siTP53 and TP53L MCF7 cells, thus indicating that it is indeed
242 nuclear AGO2 which is responsible for the increased viral gene expression. Overall, we
243 discovered a clear link between nuclear AGO2 localization and viral mRNA levels, indicating
244 a pro-viral role of nuclear RNAi.
245
246 **Nuclear AGO2 downregulates antiviral type-I interferon response**
247 Upon IAV infection innate immunity is the first line of host defense, and the immediate
248 immune response is mediated by type-I IFN [37]. Type-I IFN are rapidly produced by infected
249 cells to trigger an antiviral state, thus inhibiting viral replication [38]. Given that AGO2:p53
250 nuclear translocation increased viral titer, we therefore hypothesized that AGO2:p53 nuclear
251 translocation might have a proviral function by downregulating innate immune responses.
252 First, we assessed the steady state levels of IFN-Is by measuring *IFNB* mRNA levels [39] by
253 qRT-PCR in HEK293 vs HEK293T cells. Interestingly, we observed significantly higher levels
254 of *IFNB* in HEK293 cells (nuclear AGO2 negative) compared to HEK293T cells (nuclear
255 AGO2 positive) (**Fig 5A**), indicative of distinct IFN-I regulation between the two cell lines.
256 Subsequently, we examined the dynamics of *IFNB* levels in HEK293 cells at three
257 distinct time points following PR8 infection. We observed an initial increase in *IFNB* at 2 hours
258 post-infection, followed by a decrease at 8- and 16-hours post-infection, where the levels were
259 lower than baseline (**Fig 5B**). In the same time frame mentioned above, we also performed
260 biochemical fractionation assays. Strikingly, the decline in *IFNB* production coincided with
261 the translocation of AGO2 into the nucleus at 8 hours post-infection, suggesting a potential
262 contribution of nuclear AGO2 in the downregulation of antiviral IFN-I production (**Fig 5C**).
263 To explore whether the regulation of IFN-I expression is a general feature in cells
264 positive for nuclear AGO2, we measured *IFNB* in WT and TP53L MCF7 cells. Notably, we
265 observed low levels of *IFNB* expression in WT MCF7 cells (with nuclear AGO2), while the

266 TP53L MCF7 cells, lacking nuclear AGO2, displayed significantly higher *IFNB* levels (**Fig**
267 **5D**). Having observed that the lack of p53, and consequent lack of nuclear AGO2, allows for
268 the expression of *IFNB*, we next reasoned that we should be able to recapitulate the above
269 observation in nuclear AGO2 positive cells when p53 is monomeric and AGO2:p53 complex
270 is excluded from the nucleus (**Fig 3D,F**). To investigate the impact of p53 monomerization on
271 IFN-I expression we measured *IFNB* levels in HEK293T cells treated with ATO and observed
272 a significant increase in *IFNB* (**Fig 5E**), which is likely due to the exclusion of AGO2:p53 from
273 the nucleus. Furthermore, as expected, HEK293T cells and MCF7 cells treated with ATO and
274 infected with IAV exhibited reduced viral gene expression (**Fig 5F,G**), linked with rescued
275 *IFNB* levels (**Fig 5H,I**). In addition, to further elucidate the role of AGO2:p53 axis in regulating
276 *IFNB* expression, we performed siRNA-mediated knockdown of *AGO2* and *TP53* in HEK293T
277 cells and measured *IFNB* mRNA levels (**Fig 5J**). Silencing either *AGO2* or *TP53* led to an
278 increase in *IFNB* mRNA levels (**Fig 5J**). Importantly, p53 nuclear localization is not
279 compromised with AGO2 silencing (**Fig 3H,I**) hence suggesting a direct role of nuclear AGO2
280 in *IFNB* regulation.
281 Type-I IFNs, which are produced by infected cells, trigger a signaling cascade that
282 timely leads to an antiviral state by promoting the expression of interferon simulating response
283 elements (ISRE), via IFNAR1 and IFNAR2 stimulation [38]. Therefore, we next wanted to gauge
284 whether increase in *IFNB* triggered downstream activation of IFNAR-mediated ISRE pathway
285 after IAV infection. In HEK293 cells infected with IAV, we noted a slight reduction in *IFNAR2*
286 expression, coinciding with the nuclear translocation of AGO2 (**Fig 5K**). Importantly, silencing
287 of *AGO2* by siRNA significantly reversed this phenomenon (**Fig 5K**). To assess the
288 downstream effects of interferon response, we measured the expression of ISRE. Utilizing a
289 luciferase reporter assay in both IAV-infected and control HEK293 cells, we found that the
290 ISRE expression was significantly increased in IAV-infected cells only when AGO2 was
291 silenced (**Fig 5L**). Taken together, our findings support the notion that nuclear localization of
292 AGO2 acts as a mechanism to suppress the induction of antiviral IFN-I and its signaling
293 cascade, thereby facilitating viral infection. This resistance mechanism utilized by viruses
294 highlights the intricate interplay between viral pathogens and the host immune response.
295
296 **Type-I-IFN-pathway-related genes and *TRIM71* are negatively regulated by nuclear**
297 **RNAi.**
298 As nuclear AGO2 translocation correlated with diminished interferon expression and enhanced
299 viral gene expression, we hypothesized that nuclear RNAi may directly suppress type-I IFNs.

300 First, to comprehensively understand the transcriptional dynamics of host cellular responses
301 during IAV infection, we conducted RNA sequencing experiments in HEK293 cells post-IAV
302 infection. The results of principal component analysis (PCA) demonstrated that IAV infection
303 elicited a distinctive transcriptomic profile in HEK293 cells (**Sup Fig 4A**). Further, we
304 identified 1773 differentially upregulated and 352 differentially downregulated RNA
305 transcripts in response to IAV infection (**Sup Fig 4B** and **Sup Table 2**). As expected, gene
306 ontology (GO) analysis of biological processes revealed that PR8 infection significantly
307 induced defense response and regulation of immune effector processes (**Sup Fig 4C**).
308 Upregulated genes, associated with inflammation and innate immunity, included *ARRD3,*
309 *ITGB1BP2, SOCS1, SOCS3, TRIM72, GADD45B,* and *CD68* (**Sup Fig 4B**). Notably, among
310 the upregulated genes, *TRIM72*, and *SOCS1* emerged as potential inhibitors of the IFN-I
311 response, with reported interactions with RIG-1, IFNB, and IFNAR, respectively [40-42].
312 To explore the role of nuclear RNAi and define AGO targets at nucleotide resolution,
313 we employed fPAR-CLIP assay [43] in two replicas in HEK293 cells with or without IAV
314 infection, from either cytoplasmic or nuclear fractions and using the T6B peptide, which
315 recognizes all four AGOs, to isolate AGO-bound RNAs [44] (**Sup Fig 4D**). Overall, we identified
316 41 743 cytoplasmic and 12 119 nuclear AGO1-4 binding sites in control cells (**Fig 6A**). At 16
317 hours post IAV infection, we identified 30 083 cytoplasmic and 78 665 nuclear AGO1-4
318 binding sites, a remarkable 6.5 fold increase of nuclear AGO-targets (**Fig 6A**). A clear
319 difference in control *vs* IAV-infected nuclear AGO target occupancy was also evident by PCA
320 analysis (**Sup Fig 4E**). Finally, when mapping the distribution of fPAR-CLIP sequence reads
321 across target RNAs little changes were observed in AGO target occupancy obtained from the
322 cytoplasmic fraction, with or without viral infection (**Fig 6A**). Contrary, the striking increase
323 in nuclear AGO transcript clusters, suggested that, once AGOs enter the nucleus, they expand
324 their binding preferences and interact with the pre-mRNA sequence. Indeed, the predominant
325 increase of target occupancy was on intronic sites, but also at 3'UTR and CDS regions within
326 the nucleus (**Fig 6A**).
327 Next, we sought to investigate what targets the AGOs regulate upon viral infection. To
328 better visualize shifts in AGO-binding within the different cellular fractions, we plotted the
329 fPAR-CLIP signal, for all coding genes, in control (- virus) *vs* IAV-infected (+ virus) cells.
330 While dots on the axis indicate unique binders, a shift from the dashed line (x=y) denotes
331 enrichment in the number of AGOs binding to each transcript and/or the number of bound
332 transcripts. The resulting scatter plots highlighted no changes in the cytoplasmic environment
333 (**Fig 6B**) but a surge in AGO binding, within the nucleus, post-infection (**Fig 6C**). Taken

334 together, the results demonstrate that, upon IAV infection, not only is there an enrichment in
335 nuclear AGO targets, but that more AGOs are bound to each transcripts, upon viral infection.
336 Furthermore, to understand the effect of AGO-binding, we analyzed the best AGO
337 binding targets by cumulative distribution analysis, in relation to RNAseq experiment (**Sup**
338 **Fig 4B**). Here, a shift of the cumulative distribution function (CDF) curve to the left means
339 that a higher proportion of AGO targets are effectively suppressed, indicating that the RNAi
340 machinery is active and efficient. Consistent with the canonical function of cytoplasmic RNAi,
341 we found that AGO1-4 suppressed its best binding targets in the cytoplasm equally, regardless
342 of IAV infection (**Fig 6D,E**). On the contrary, in the control nuclei, AGO1-4 the differences in
343 fold change between AGO targets and non-targets are minor, as evident by the CDFs and the
344 fact that AGOs are not present in the nucleus in steady state HEK293 cells (**Fig 6F**). However,
345 we observed potent negative gene regulation of nuclear AGO fPAR-CLIP targets, after IAV
346 infection (**Fig 6G**). Further, analysis of the top 10% fPAR-CLIP nuclear targets against
347 COVID-19 related gene sets [45] by enrichment analysis [46-48] identified these genes among the
348 most downregulated genes after COVID-19 infection in ferrets and hamsters (**Sup Fig 4F**).
349 Our previous data (**Fig 5**) suggested that AGO2 nuclear translocation correlated with a
350 decrease in type-I IFN pathway, which is crucial for antiviral responses. To test whether
351 nuclear AGOs had a direct effect on genes specifically involved in type-I IFN response, we
352 highlighted targets specifically involved in IFN-Is response [49] in the scatter plot and performed
353 CDF using those specific targets (**Fig 6H,I**). Indeed, 124 out of 131 genes were nuclear AGO
354 targets and were substantially downregulated by nuclear RNAi (**Fig 6H,I**).
355 To further gain insight into what genes AGO1-4 targets in the nucleus during viral
356 infection, we ranked the fPAR-CLIP targets of the AGOs (**Fig 6J, Sup Table 3**). Notably,
357 among the top AGO-bound transcripts in the nuclear fraction from viral-infected cells, three of
358 the top ten targets were in the 3'UTR and intronic regions of *LRP1B*, *TRIM71*, and *SOCS5* (**Fig**
359 **6J**). These molecules are well known for their significant roles in the immune response [11,50,51].
360 Of particular interest is *TRIM71* (also referred to as LIN41), renowned for its positive influence
361 on the IFNβ and ISRE responses but also directly inducing AGO2 and p53 degradation
362 processes [11,52,53]. Further elucidation from a STRING analysis revealed that AGO2
363 predominantly interacts with TRIM family proteins that plays a positive role in type-I
364 interferon pathway, especially with TRIM56, and TRIM71 (**Sup Fig 4G**). Our fPAR-CLIP
365 data, interpreted via the IGV software [54], clearly showed an enhanced AGO2 binding to
366 *TRIM71*, *LRP1B*, *SOCS5*, *IFNAR2* and *TRIM56* 3'UTR site following IAV infection,

367 compared to controls (**Fig 6K, Sup Fig 4H-K**). Corroborating this observation, post IAV-
368 infection, there was a significant decrease in TRIM71 and IFNAR2 protein levels (**Fig 6L, Sup**
369 **Fig 4L**).
370 Our experimental data indicated that IAV infection promotes AGO2 nuclear
371 translocation, and the fPAR-CLIP results suggest two possible complimentary functions of
372 nuclear RNAi. 1) Direct silencing of genes involved in the type-I IFN pathways and, 2)
373 targeting of TRIM71 to block its direct effect on IFN response but also to prevent AGO2 and
374 p53 degradation. To experimentally test the latter, we overexpressed TRIM71 transiently in
375 IAV-infected HEK293; indeed, we observed a marked reduction in nuclear AGO2 levels (**Fig**
376 **6M**). This coincided with diminished p53 levels, aligning with the recognized role of TRIM71
377 as a p53 and AGO2 E3 ligase [11,52,53]. Consequently, there was an increase in *IFNB* (**Fig 6N**)
378 and other type-I IFN related genes mRNA levels (**Sup Fig 4M**), and a decrease in viral mRNA
379 (**Fig 6O**), attributable to the innate immune function of TRIM71 and decreased presence of
380 nuclear AGO2.
381 These insights suggest a nuanced viral strategy that involves AGO2-mediated gene
382 silencing combined with TRIM71 and IFNAR2 targeting. The culmination of these actions
383 dampens the type-I IFN pathway, allowing the virus to adeptly evade host immune defenses.
384 In summary, our integrated approach combining RNA sequencing and fPAR-CLIP
385 demonstrates that nuclear AGO2 is crucial for the virus to subvert host immune responses and
386 to ensure a successful infection.
387
388 ***In vivo* arsenic trioxide treatment reverses AGO2 nuclear translocation in lungs and**
389 **potentiates innate immune functions.**
390 Our data demonstrates that AGO2 suppresses type-I IFN in the nucleus and that p53 is essential
391 to mediate AGO2 nuclear translocation. To confirm these mechanisms *in vivo*, we intranasally
392 (i.n.) administered IAV-PR8 to wild-type C57BL/6 mice. Lung tissues were harvested on days
393 1 and 3 post-infection (d.p.i.) (**Fig 7A**). As expected, mice infected with IAV exhibited
394 markedly elevated viral mRNA levels in lung tissues when compared to controls at 3 d.p.i. (**Fig**
395 **7B; Sup Fig 5A**). Next, we isolated single cells from both control and IAV-infected lung
396 tissues for biochemical fractionations assays. Healthy lung cells predominantly showed
397 cytoplasmic AGO2 distribution. In contrast, a notable nuclear accumulation of AGO2 was
398 observed in response to IAV infection (**Fig 7C**). To exclude that the positive AGO2 signal we
399 observed in the nuclear fraction was due to the influx of immune cells in the infected lungs [55],
400 we carried out a negative selection of $CD45^+$ immune cells. We found that AGO2 translocated

401 to the nucleus in both CD45$^+$ and CD45$^-$ cells, thus confirming that IAV infection induced
402 AGO2 translocation in the epithelial and endothelial cells (**Sup Fig 5B**), thus providing *in vivo*
403 evidence supporting IAV-mediated AGO2 nuclear translocation.
404 To further explore the effects of AGO2 in the nucleus upon viral infection, we
405 administered the FDA-approved ATO treatment known to monomerize p53 and destabilize
406 nuclear AGO2 (**Fig 3**). Mice received 0.15mg/kg of ATO for 4 days, starting one day before
407 infection, and lungs were harvested at 3 d.p.i. (**Fig 7D**). Two control groups received either
408 daily vehicle injection or daily ATO injection, without infection. The experimental groups
409 received either daily vehicle injection + IAV i.n. infection or daily ATO injection + IAV i.n.
410 infection. At 3 d.p.i. single cells were isolated from lungs. It is important to note that it was not
411 possible to fully assess the efficacy of the ATO treatment *in vivo*. Indeed, when using nuclear
412 p53 levels, as a proxy of efficacy, ATO treatment was successful in only ~50% of treated mice.
413 However, whenever p53 was excluded from the nucleus, we observed that also AGO2 was
414 excluded regardless of IAV-infection, underscoring the critical role p53 plays in nuclear AGO2
415 accumulation also *in vivo* (**Fig 7E**). Therefore, for our subsequent analysis we only considered
416 mice where ATO treatment excluded p53 from the nucleus. Indeed, we observed a trend
417 towards reduced viral mRNA levels and ~1-log reduction of infectious virus in the lungs of
418 ATO-treated mice (**Fig 7F,G**). TRIM71 was the second top target from our nuclear fPAR-
419 CLIP and a negative regulator of AGO2 and IFN levels. Interestingly, ATO treatment in IAV-
420 infected mice enhanced *Trim71* levels (**Fig 7H**), in line with all the results obtained *in vitro*.
421 Furthemore, ATO-treated, IAV-infected mice had increased *Ifnb* and *Ifnar2* mRNA levels (**Fig**
422 **7I,J**), again supporting the *in vitro* mechanistic insights. Taken together, we unraveled a new
423 layer of regulation of IAV infection and propose that targeting either p53 or nuclear AGO2
424 might serve as a potential therapeutic avenue for IAV modulation.
425
426 **DISCUSSION**
427 Unveiling mechanisms of viral resistance is crucial for designing effective new therapies to
428 alleviate disease. Here, by combining classical biochemical fractionation experiments with
429 fPAR-CLIP to identify the precise targets of nuclear AGO2 and *in vivo* mouse models we
430 discovered complex events leading to increased viral replication. We identified viral infection
431 as a potent trigger for nuclear AGO2 translocation, in complex with p53. In the nucleus, AGO2
432 suppresses innate immune genes thus favoring viral replication. By pinpointing the molecular
433 mechanisms involved, we could use the FDA approved drug arsenic trioxide to reverse AGO2
434 nuclear localization, increase innate immune response and lower viral infectivity.

435 In our study, we highlighted how certain viral components—specifically the large T
436 antigen from SV40 (a DNA virus) and NS1 from IAV (an RNA virus)—induce the nuclear
437 accumulation of both p53 and AGO2 (**Fig 2D,E**). This adds to the multiple proviral roles of
438 NS1 [56]. A limited number of previous reports already identified nuclear presence of AGO2
439 upon IAV infection [22,57], however both utilized cell lines (A549 and HEK293T) which are
440 already nuclear-AGO positive at steady state [25], thus complicating the interpretation of the
441 results. Herein, by using HEK293 cells, which are nuclear AGO negative at steady state, we
442 could better mimic what happens in mouse lungs. Indeed, also Wang et al described nuclear
443 accumulation of AGO2, mediated by NS1, and associated with increased virulence *in vivo*, but
444 did not provide any mechanistic explanation of the phenomenon [57]. In general, the translocation
445 of AGO2 from the cytoplasm to the nucleus is an intricate, dynamic process, elicited by a
446 spectrum of cellular stressors, including, but not limited to, DNA damage, activation of
447 oncogenes, and viral infections [20,57,58]. In our investigation, we observed nuclear accumulation
448 of AGO2 specifically in response to high-titer viral infections (MOI=10). This phenomenon
449 was concomitant with the elevated expression of *GADD45B* (log2 fold change: 3.129), a key
450 player in DNA damage repair and cellular senescence. It's noteworthy that infections with high
451 MOI have been linked to the stimulation of cellular senescence [59]. Fascinatingly, the nuclear
452 accumulation of p53 is also a characteristic feature of senescent cells [60]. In addition, here we
453 demonstrate that p53 is necessary to stabilize AGO2 in the nucleus. We postulate that the
454 tandem tryptophan-binding pockets within the PIWI domain of AGO2 may serve as interaction
455 sites with the flexible N-terminus of p53, characterized by three tryptophan residues: Trp23,
456 Trp53, and Trp91 (**Fig 3C,D**). While it was previously reported that, in cancer, p53 and AGO2
457 interacted within the cytoplasm [61], here we further revealed the strong interaction within the
458 nucleus and complement it by demonstrating that the tetramerization of p53 may enhance the
459 stability of nuclear AGO2 (**Fig 3K**). p53 N-terminus, containing transactivation domains and
460 multiple phosphorylation sites, can also modulate DNA binding, potentially influencing its
461 interaction with proteins like MDM2, a p53 E3 ligase [62]. Further research is needed to
462 understand how AGO2-p53 interactions impact p53's DNA binding and protein stability.
463 Here, we further elucidated the functional consequences of AGO2 nuclear
464 translocation. In general, RNAi function during viral infections is intricate and hotly debated:
465 it has been shown that RNAi can inhibit viral replication and augment the host immune
466 response, thus acting as an anti-viral factor, or promote viral replication and host immune
467 response evasion as a pro-viral factor [4,7,63,64]. While we have not studied in detail the presence
468 of viral small RNAs in our samples and the potential impact of direct RNAi against IAV,

469 indirect evidence suggest this is not to play a major role here. Indeed, by silencing p53 we did
470 not affect overall AGO2 levels, nevertheless we measured differences in viral mRNA, which
471 was not compatible with a direct antiviral role of RNAi. Notably, diminished levels of AGO2
472 mRNA are reported in COVID-19 patients in comparison to healthy individuals [65]. Moreover,
473 AGO4, another effector in the RNAi/miRNA pathway, has illustrated antiviral properties in
474 mammals [66]. We noted an increase in nuclear AGO4 following PR8 infection, necessitating
475 further studies to elucidate its impact on the innate immune system. Together, the effects of
476 AGO2 on viral infection can be governed by diverse variables such as viral quantity, host cell
477 type, expression level and subcellular localization of AGO2. Thus, a nuanced understanding of
478 the viral infection context is essential to decrypt the varied roles of AGO2 in viral infections.
479 Our experimental data, combined with analysis of nuclear AGO targets by fPAR-
480 CLIP strongly indicated that nuclear AGO2 has a direct role in silencing the antiviral interferon
481 response in infected cells. This finding is consistent and mechanistically explains, several
482 sparse observations from previous studies: Backers *et al*. showed that in the absence of small
483 RNAs, *in vivo* RNA virus infection reached lower titers due to reduced repression of antiviral
484 genes; further, Seo *et al*, also postulated that inactivation of RISC would facilitate antiviral
485 response [6,7]. Furthermore, it was recently demonstrated that single cells infected with high MOI
486 had higher repression of innate immune genes, as compared to single cells infected with lower
487 MOI [67]. Yet another study identified AGO2 as negative regulator of IFNβ signaling and another
488 reported that p53 had direct impact on IFN-regulated genes, without relying on its
489 transcriptional activity [57,68]. Finally, it was also shown that Dicer-2 accumulation had a
490 negative effect on IFNβ signaling in human cells [69]. Altogether, the studies summarized
491 provided several pieces of information which we confirmed and expanded here in a
492 comprehensive mechanistical model, which includes a nuclear function of AGO2.
493 In our quest to understand the molecular details by which IAV promotes AGO2:p53
494 accumulation within the nucleus, we utilized fPAR-CLIP to scrutinize the silencing targets of
495 nuclear AGO. Beside the IFN-pathways genes, discussed above, we underscored the pivotal
496 roles of nuclear E3 ligases, notably TRIM71 and MDM2. These ligases are instrumental in
497 determining the degradation pathways of AGO2 and p53, thereby influencing their nuclear
498 stability [52,70]. Our observations also underlined nuclear AGO targeted entities which are crucial
499 for p53 stability and its export to the cytosol, namely MDM2 and XPO1. Together, our results
500 indicate that the virus-induced presence of nuclear AGO2 appears to facilitate the aggregation
501 of AGO2:p53 in the nucleus and thus serving the dual role of stabilizing the complex and to

502 repress the antiviral immune response. TRIM71 was one of the top targets and, beside its E3
503 ligase role, it has not been extensively studied; neverthelessm it has been reported as immune
504 enhancing protein, and, in a recent study, its silencing resulted in increased SARS-CoV-2 viral
505 titers [11,71]. Here we further validated TRIM71 antiviral role and showed it to be associated with
506 viral titer, IFN response and AGO2 stability both *in vitro* and *in vivo*.
507 The findings from our current work elucidate how the activation of p53, induced by
508 IAV, fosters the nuclear accumulation of AGO2, subsequently leading to the suppression of
509 innate immune genes, a scenario that can aggravate the clinical outcomes of IAV infection.
510 Such insights into the interplay between p53 activation and AGO2 translocation underscore the
511 potential of targeting p53-mediated AGO2 nuclear translocation as a viable therapeutic
512 strategy, as we have demonstrated using arsenic trioxide. Overall, our results could open new
513 avenues to slow down the progression and reduce the severity of viral infections.
514
515 **LIMITATIONS OF THE STUDY**
516 Here we demonstrated a link between nuclear AGO2:p53 translocation, the suppression of IFN
517 response and viral loads upon IAV infection. Although likely, we can not generalize our results
518 to other viral pathogens and/or other disease models, like cancers, which show increase
519 accumulation of nuclear AGO2. In addition, while we have individually silenced p53 and
520 AGO2 and shown that the majority of the effects we observe are due to AGO2, we cannot fully
521 exclude that stabilized nuclear p53 will impact transcription thus influencing some of our
522 results. Finally, it is extremely difficult to gauge the efficacy of ATO treatment *in vivo*, thus
523 rendering the interpretation of mouse experiments complicated.
524
525 **ACKNOWLEDGMENTS**
526 This work was funded by the European Research Council (ERC-StG, B-DOMINANCE, grant
527 no. 850638 to DA); the Swedish Research Council (grant no. 2021-01164, 2021-01165 to DA
528 and grant number 2019-01855 to AS); the Knut and Alice Wallenberg Foundation (grant no
529 2021.0033 to DA and grant no PAR 2020/228 to AS); the Swedish Society for Medical
530 Research (grant no S19-0019 to AS) and the University of Gothenburg. J.O.W. is financially
531 supported by the Knut and Alice Wallenberg Foundation as part of the National Bioinformatics
532 Infrastructure Sweden at SciLifeLab. We are grateful to Dr. Marianne Farnebo (Karolinska
533 Institutet) for the generous contribution of TP53L expressing MCF7 cells. We would like to
534 thank the staff at the Experimental Biomedicine (EBM) core facility at the University of

535 Gothenburg for animal management. The sequencing was performed at the National Genomics
536 Infrastructure (NGI), which is supported by the National Institutes of Health (NIH).
537

538 **AUTHOR CONTRIBUTIONS**

539 H.-C.H. designed the experiments, performed the experiments, analyzed data, and wrote the
540 manuscript. D.A., D.G.A, and J.O.W. analyzed the NGS sequencing data. V.L. and I.N
541 generated the PAR-CLIP libraries. C.F. performed immunofluorescent experiments. K.S.,
542 A.A.H.P., and C.W. performed animal experiments and analyzed data. V.I.S. provided
543 scientific input and feedback on the manuscript. D.A. and A.A.S. supervised the entire project,
544 designed the experiments, analyzed data, and wrote the manuscript. All authors contributed to
545 the manuscript
546

547 **DECLARATION OF INTEREST**

548 The authors declare no competing interests.
549

550 **METHODS**

551 **Mice and Ethical Statement**

552 All the experiments were conducted according to the protocols (Ethical permit numbers
553 1666/19, 38/23 and 2071/19) approved by regional animal ethics committee in Gothenburg.
554 Female, 8-12 weeks old C57BL/6 mice were purchased from Janvier, France. They were
555 housed in the specific pathogen-free animal facility of Experimental Biomedicine Unit at the
556 University of Gothenburg.
557

558 **Cell culture**

559 HEK293 (ATCC, CRL-1573), HEK293T (ATCC, ACS-4500), MCF7 (ATCC, HTB-22),
560 MCF7 TP53L (kind gift from Dr. Marianne Farnebo, Karolinska Institutet) cell lines were
561 cultured in Dulbecco's modified Eagle's medium (DMEM) (Gibco, 11995065), supplemented
562 with 10% fetal bovine serum (FBS) (Gibco, 11573397) and 100 U/ml penicillin-streptomycin
563 (Gibco, 11548876) in a humidified incubator at 37°C and 5% CO2. The SK-N-BE(2) cell line
564 was cultured in the same medium, but with the addition of 1% non-essential amino acids
565 (Gibco, 11140050).
566

567 **Whole cell lysate and biochemical fractionation**

568 To extract whole cell lysates, the cells were first washed with cold 1xPBS and then lysed on
569 ice with RIPA lysis buffer (50 mM Tris-HCl, pH 7.6, 150 mM NaCl, 1 mM EDTA, 1% NP-
570 40, 1% sodium deoxycholate, 0.1% sodium dodecyl sulfate) supplemented with a protease
571 inhibitor cocktail (Merck Millipore, 04693132001). Samples were cleared with centrifugation
572 at 12 000 *g* for 20 minutes and the supernatant collected. Biochemical fractionation assay was
573 done as previously described [25]. Briefly, cell pellets were gently dissolved in a hypotonic lysis
574 buffer (10 mM Tris-HCl, pH 7.6, 10 mM NaCl, 3 mM $MgCl_2$, 0.3% NP-40, 10% Glycerol),
575 supplemented with a protease inhibitor cocktail, with gentle pipetting up and down and
576 collected with centrifugation for 2 minutes at 200 g. The supernatant was cleared with
577 centrifugation at 12 000 *g* for 20 minutes and the supernatant stored as the cytoplasmic fraction.
578 The remaining nuclear pellet was washed 3 times with the hypotonic lysis buffer and each time
579 collected by centrifugation for 2 minutes at 200 g. Each time the supernatant was discarded.
580 From the remaining pellet, the nuclear proteins were extracted using a nuclear lysis buffer (20
581 mM Tris-HCl, pH 7.6, 150 mM KCl, 3 mM $MgCl_2$, 0.3% NP-40, 10% Glycerol) supplemented
582 with protease inhibitor cocktail. The lysate was sonicated twice for 10 seconds each time at
583 60% amplitude (Sonics, VCX130). The nuclear fraction was cleared with centrifugation at
584 12 000 *g* for 20 minutes and the supernatant collected. Protein concentration was measured
585 using Bradford Reagent (B6916, Sigma Aldrich).
586
587 **Western blotting**
588 After protein extraction, as described above, 5-20 ug of protein were used for western blot
589 experiments. Protein samples were run on 4-12% Bis-Tris gels and transferred onto
590 Nitrocellulose membrane (Cytiva, 1060000). Proteins of interested were analyzed by
591 hybridization with their corresponding antibodies (see below) and visualized by
592 chemiluminescence using Thermo Scientific SuperSignal™ West Dura Extended Duration
593 Substrate (ThermoFisher, 34076).

FLAG (Merck, M8823)
HA (Sigma, H9658)
AGO1 (CST, 5053S)
AGO2 (Abcam, ab32381)
AGO2 11A9 for IF (Merck, MABE253)
AGO3 (CST, 5054)
AGO4 (CST, 6913S)

Histone H3 (CST, 44995)
p53 (Abcam, ab1101)
p53 (Santa cruz, sc-126)
p53 (ThermoFisher, MA5-11296)
Lamin B1 (Abcam, ab16048)
Lamin A/C (Santa cruz, sc-376248)
GAPDH (Abcam, ab9485)
SV40 (Santa cruz, sc-147)
mCherry (Santa cruz, sc-101529
Ubiquitin (Santa cruz, sc-8017).
TRIM71 (ThermoFisher, PA5-19281)
IFNAR2 (ThermoFisher, PA5-28303)
anti-rabbit IgG, HRP conjugate (Sigma, GENA934)
anti-mouse IgG, HRP conjugate (Sigma, GENA931).
anti-goat IgG, HRP conjugate (ThermoFisher, 10466033)
snti-sheep IgG, HRP conjugate (Merck, AP147P)

Plasmid transfection

Plasmids encoding the Influenza A virus components PB1, PB2, NP, M, HA, NA, NS1, PA and mCherry-NS1 were a kind gift from Dr. Ivan Kosik (NIH, USA). The SV40 Large T antigen and HA-TRIM71 were purchased from Addgene (plasmid # 136616 and #52717, respectively). 3 µg of plasmid was used for transient transfection using X-tremeGENE™ HP DNA Transfection Reagentreagent (Roche, 6366236001) following the manufacturer's instructions.

Viral infection in cells

1 million HEK293 cells were seeded in 10 cm dishes. Cells were allowed to attach for 8 hrs and were infected with PR8 with different MOI (0.1 to 50) for 16 hrs in serum free media. Cells were collected by trypsinization.

Viral titer determination from infected lungs

MDCK cells were seeded at 50,000 cells/well in 96-well plates. After overnight incubation, cells were washed twice with PBS. Harvested lungs were placed in PBS at a constant w/v ratio.

611 Homogenized lungs were 10-fold diluted starting 1:10 in infection media (DMEM containing
612 0.1% BSA (fraction V; Roche), 10 mM HEPES (Corning), 500 µg/ml gentamicin (Gibco), and
613 1 µg/ml TPCK trypsin (Worthington) and incubated on MDCK cells. After 3 days cytopathic
614 effect was visualized after crystal violet staining and $TCID_{50}$ titer was calculated using the
615 Spearman and Karber method.
616
617 **Immunofluorescence staining and microscopy**
618 To perform immunofluorescence assay, HEK293 cells were either transfected with mCherry-
619 NS1 or infected with PR8-IAV, as described above, for 16 hours. Alternatively, HEK293 cells
620 were infected with mCherry-PR8 for 16 hours. Cells were washed with PBS and fixed with 4%
621 buffered formalin for 15 minutes at room temperature. Cells were then washed twice with PBS
622 and blocked with 5% BSA in PBS for 1 hour at room temperature. Finally, cells were incubated
623 with 1:200 AGO2 (Merck, MABE253) overnight. The next day cells were washed 3x with
624 PBS and probed with secondary antibodies: 1:2000 Alexa Fluor® 488 Goat Anti-Rat IgG
625 (Invitrogen, 10729174) or 1:1000 phalloidin (Invitrogen, 10643853) for 2 hours at room
626 temperature. To visualize the cell nuclei, 4',6-diamidino-2-phenylindole (DAPI; Invitrogen,
627 D3571) was added for 5 minutes in the dark. Slides were mounted using 10 µl Prolong Diamont
628 (Invitrogen, 15372192). Confocal images were taken on a Zeiss LSM780 and the images were
629 analyzed using ImageJ® software and Affinity Designer®.
630
631 **Doxorubicin treatment**
632 Doxorubicin (Biotechne (Tocris), 2252) was dissolved in dimethyl sulfoxide (DMSO) to
633 prepare a 1 mM stock solution. The stock solutions were stored at -20°C and diluted in the
634 culture medium to 1 µM final concentrations. Cells were incubated with doxorubicin for 24
635 hours.
636
637 **Immunoprecipitation assays and AGO protein affinity purification with T6B peptide**
638 Immunoprecipitation was carried out in 1-3 mg of protein lysate and 2 µg of anti-AGO2, anti-
639 IgG, or anti-p53 antibodies. For purification of AGO1-4, 400 µg Flag-tagged T6B peptide was
640 used [44]. Dynabead Protein G beads (10004D, ThermoFisher) or anti-Flag M2 beads (M8823,
641 Millipore) were conjugated with either antibodies or T6B peptide, respectively, for 4 h, washed
642 and incubated with protein lysates. Next, beads were washed three times with RIPA buffer and
643 bound proteins were eluted at 95°C for 5 min in 3× SDS Laemmli buffer and assessed by
644 western blot. The pull-down efficiency was confirmed by western blot.

645 **p53 mutagenesis**

646 The plasmid encoding amino acids 1-393 of the p53 protein with a FLAG tag at the C-terminus
647 (Addgene plasmid #10838) was used as a template for site-directed mutagenesis to delete the
648 N-terminal regions spanning amino acids 1-31, 1-62, or 1-93. The resulting PCR products were
649 cloned into the pcDNA3.1 expression vector (Invitrogen, v79020). The final constructs
650 encoded truncated p53 proteins with a FLAG tag starting at amino acids 32, 63, or 94,
651 respectively. The pcDNA3 constructs were used for transient transfection in HEK293 cells
652 using an X-tremeGENE HP DNA Transfection Reagent (Roche, 6366236001according to the
653 manufacturer's instructions. The expression of the full-length and truncated p53 proteins were
654 verified by western blotting using an anti-FLAG antibody (Merck, M8823).

655

656 **Arsenic trioxide (ATO) treatment**

657 Arsenic trioxide (Merck, 202673-5G) was dissolved to 100 mg/ml stock solution in NAOH
658 which was further diluted in DMEM to 1 mg/ml. The stock solutions were stored at -20°C and
659 diluted in the culture medium to 0.01, 0.1 or 0.5 μg/ml concentrations before use. Cells were
660 incubated with ATO for 24 hours.

661

662 **siRNA Gene Silencing of AGO2 and TP53**

663 Small interfering RNA (siRNA) targeting human *AGO2* (siRNA ID: s109013 and ID s25931),
664 *TP53* (siRNA ID s607), and scramble control siRNAs (siRNA ID: 4390843) were purchased
665 from ThermoFisher Scientific. Human HEK293T, MCF7, or SK-N-BE(2) cells were
666 transfected with the siRNAs using Lipofectamine RNAiMAX Transfection Reagent
667 (ThermoFisher Scientific, #13778030) according to the manufacturer's instructions. The cells
668 were harvested 48 hours after siRNA transfection to evaluate AGO2 or p53 knock-down
669 efficiency by quantitative RT-qPCR and protein level by western blotting.

670

671 **MG132 treatment and ubiquitination assay**

672 MG132 (ThermoFisher, 15465519) were dissolved in dimethyl sulfoxide (DMSO) to prepare
673 a 10 mM stock solution. The stock solutions were stored at -20°C and diluted in the culture
674 medium to 40 μM concentrations before use. Cells were treated with MG132 or DMSO only
675 for 4 hours. Following the treatment, cells were lysed and/or fractionated and assessed by
676 western blotting.

677

678

679 **Structure modelling**

680 To model the structures of p53 (AF-P04637-F1), we downloaded their atomic coordinates from
681 the AlphaFold2 database [72]. We used the PyMOL Molecular Graphics System, Version 2.3.4
682 (Schrödinger, LLC, https://pymol.org/2/) to visualize and modify the structure figures.

683

684 **Real-time quantitative PCR (RT-qPCR)**

685 To analyze gene expression levels, real-time quantitative PCR (RT-qPCR) was performed on
686 four different cell lines: HEK293, HEK293T, MCF7 and MCF7 TP53L. Total RNA was
687 isolated from each cell line using the Quick-RNA Miniprep Kit (ZYMO Research, R1055)
688 following the manufacturer's instructions. To generate cDNA, 1 μg of total RNA was used in
689 a reverse transcription reaction with the iScript cDNA Synthesis kit (Bio-Rad, 1708891)
690 according to the manufacturer's instructions. The RT-qPCR reactions were performed in a 10
691 μL mixture, consisting of 1x iQ™ SYBR® Green supermix (Bio-Rad, 1708880), 0.5 μmol/L
692 of each primer, and 10 ng of cDNA template. The RT-qPCR result was acquired by CFX
693 Connect Real-Time PCR Detection System (Bio-Rad) using the following primers:

694 AGO2 forward: 5'- CAAGTCGGACAGGAGCAGAAAC-3'.

695 AGO2 reverse: 5'- GACCTAGCAGTCGCTCTGATCA-3'.

696 P53 forward: 5'- CCTCAGCATCTTATCCGAGTGG-3'.

697 P53 reverse: 5'- TGGATGGTGGTACAGTCAGAGC-3'.

698 IFNA forward: 5'- AGAAGGCTCCAGCCATCTCTGT-3'.

699 IFNA reverse: 5'- TGCTGGTAGAGTTCGGTGCAGA-3'.

700 IFNB forward: 5'- CTTGGATTCCTACAAAGAAGCAGC-3'.

701 IFNB reverse: 5'- TCCTCCTTCTGGAACTGCTGCA-3'.

702 TRIM71 forward: 5'- CGAGGCATAAGAAAGCCCTGGA-3'.

703 TRIM71 reverse: 5'- GCTTGTTGAGGTTTTGCCGCAG-3'.

704 IFNAR1 forward: 5'- CGCCTGTGATCCAGGATTATCC-3'.

705 IFNAR1 reverse: 5'- TGGTGTGTGCTCTGGCTTTCAC-3'.

706 IFNAR2 forward: 5'- ACCGTCCTAGAAGGATTCAGCG-3'.

707 IFNAR2 reverse: 5'- CCAACAATCTCAAACTCTGGTGG-3'.

708 Mouse ifna2 forward: 5'- GAGCCTAGAGACTATCACACCG-3'.

709 Mouse ifna2 reverse: 5'- TACCAGAGGGTGTAGTTAGCGG-3'.

710 Mouse ifnb1 forward: 5'- GCCTTTGCCATCCAAGAGATGC-3'.

711 Mouse ifnb1 reverse: 5'- ACACTGTCTGCTGGTGGAGTTC-3'.

712 Mouse trim71 forward: 5’- AGATGAAGGCGAAGGTGGTCCA-3’.
713 Mouse trim71 reverse: 5’- GCAGGAACAGAGACTTCGCCTT-3’.
714 Mouse b-actin forward: 5’- CATCCGTAAAGACCTCTATGCCAAC-3’.
715 Mouse b-actin reverse: 5’- CAAAGAAAGGGTGTAAAACGCAGC-3’.
716 HA forward: 5’-AAGGCAAACCTACTGGTCCTGTT-3’.
717 HA reverse: 5’- AATTGTTCGCATGGTAGCCTATAC--3’.
718 NA forward: 5’- AGGCACCAAACGGTCTTACG-3’.
719 NA reverse: 5’- TTCCGACGGATGCTCTGATT-3’.
720 NP forward: 5’- AGGCACCAAACGGTCTTACG-3’.
721 NP reverse: 5’- TTCCGACGGATGCTCTGATT -3’.
722 NS1 forward: 5’- AAATCAGAAAATAACAACCATTGGA-3’.
723 NS1 reverse: 5’ - ATTCCCTATTTGCAATATTAGGCT-3’.
724
725 **Flow cytometry**
726 MCF7 and MCF7 TP53L cells were infected with PR8-NS1-mCherry at multiplicity of
727 infection (MOI) 10 for 16 hours. Cells were collected by trypsinization and resuspended in
728 FACS buffer. Cells were acquired using BD LSR II flow cytometer (BD Bioscience) to
729 measure the expression of mCherry in MCF7 and TP53L MCF7 cells. Data analysis was
730 performed using FlowJo V10 software (Treestar).
731
732 **Luciferase assay**
733 Cells were seeded 200,000 cells in 12 well dishes. The next day, the cells were transfected with
734 ISRE reporter plasmid (a gift from Dr. Chia-Wei. Li, Academia Sinica, Taiwan) or with the
735 internal control SV40 renilla plasmid (Promega) for 24 hours and subsequently infected with
736 PR8 at MOI 10 for an additional 16 hours. Cells were then collected for luciferase assay using
737 the Dual-Luciferase Reporter assay (Promega, E1910), following manufacturers´ instructions.
738 Plates were read using CLARIOstar Plate Reader (BMG Labtech).
739
740 **RNA-sequencing**
741 Total RNA was extracted from HEK293 with or without PR8 infection (MOI:10) for 16 hours,
742 using the Quick-RNA Miniprep Kit (ZYMO Research) following the manufacturer's protocol.
743 the concentration and quality of the RNA was analyzed using Agilent 2200 TapeStation
744 System. RNA samples with RNA Integrity Number higher than 8 were sent to SNP&SEQ
745 Technology Platform (NGI Uppsala, Sweden). Libraries were prepared from 300 ng RNA

746 using the Illumina Stranded Total RNA library preparation kit, including Ribo-Zero Plus
747 treatment (20040525/20040529, Illumina Inc.) according to manufacturer's instructions. For
748 indexing Unique Dual Indexes (20040553/20040554, Illumina Inc.) were used. Sequencing
749 was carried out with NovaSeq 6000 system using paired-end 150 bp read length, S4 flowcell
750 and v1.5 sequencing chemistry. As a control sequencing library for the phage PhiX was
751 included and a 1% spike-in in the sequencing run. RNAseq data were preprocessed using the
752 RNAseq nf-core pipeline [73]. Differential expression analysis was done using DEseq2 [74], on
753 genes with at least 10 reads in at least 3 samples. Genes with FDR adjusted p-value < 0.01 and
754 absolute log2 fold change > 0.5 were considered differentially expressed. Hypergeometric
755 tests, implemented in TopGO, were used to look for enriched Gene Ontology annotation among
756 the differentially expressed genes. The fraction of reads mapping to introns and other genomic
757 regions was calculated using ReSQC [75].
758
759 **Fluorescent PhotoActivatable Ribonucleoside-enhanced CrossLinking and**
760 **ImmunoPrecipitation (fPAR-CLIP)**
761 AGO fPAR-CLIP was carried out by isolating the proteins using the T6B peptide as mentioned
762 above. fPAR-CLIP library preparation, sequencing and initial data processing was performed
763 as described in [25,43] with minor modifications. Briefly, to obtain AGO proteins RNA footprints,
764 unprotected RNA was digested on beads with 1 U RNase T1 (EN0541, ThermoFisher) for 15
765 min at RT. Next, the beads were washed three times with RIPA buffer and three times with
766 dephosphorylation buffer (50 mM Tris–HCl, pH 7.5, 100 mM NaCl, 10 mM $MgCl_2$). After
767 washing, the protein-bound RNA was dephosphorylated with Quick CIP (M0525S, New
768 England Biolabs) for 10 min in 37°C. Post dephosphorylation the beads were washed three
769 times with dephosphorylation buffer and three times with PNK/ligation buffer (50 mM Tris-
770 HCl, pH 7.5, 10 mM $MgCl_2$). Following, 0,5 µM fluorescently tagged 3' adapter
771 (MultiplexDX) were ligated with T4 Rnl2(1–249)K227Q (M0351, New England Biolabs)
772 overnight at 4°C and washed three times with PNK/ligation buffer. Next, RNA footprints were
773 phosphorylated using T4 PNK (NEB, M0201S) for 30 min in 37°C and washed three times in
774 RIPA buffer. To release the proteins the beads were incubated at 95°C for 5 min in 3× SDS
775 Laemmli buffer. Next, the eluates were separated on a 4-12% SDS/PAGE gels
776 (NW04122BOX, Invitrogen) and AGO:RNA complexes visualized on the IR 680 channel
777 (Chemidoc MP system, Bio-Rad). Subsequently, appropriate AGO:RNA bands were excised
778 from the gel and protein digested with Proteinase K (RPROTK-RO, Sigma Aldrich) and
779 released RNA isolated via phenol:chloroform phase separation. Following, 5' adapter ligation

780 (MultiplexDX) was performed on the purified RNA samples with 0,5 µM of the adapter and
781 Rnl1 T4 RNA ligase (ThermoFisher, EL0021) for 1 h at 37ºC. Next, the RNA was reverse
782 transcribed using SuperScript IV Reverse Transcriptase (ThermoFisher, 18090010) according
783 to manufacturer's instructions. The libraries were amplified in a series of PCR reactions
784 performed using Platinum Taq DNA polymerase (ThermoFisher, 10966034) and size selected
785 with 3% Pippin Prep (Sage Science, CSD3010). Sequencing of the libraries was carried out on
786 Illumina NovaSeq 6000 platform. For data processing Bcl2fastq (v2.20.0), Cutadapt (cutadapt
787 1.15 with Python 3.6.4) [76], PARpipe (https://github.com/ohlerlab/PARpipe) and Paralyzer [77]
788 were used. The 3' and 5' adaptor sequences and sequencing primers used in the study are listed
789 below. For each target gene, the normalized PAR-CLIP signal was calculated as nr reads with
790 T->C conversions / (total number of PAR-CLIP reads * average TPM for target gene * 1e-6)
791

Oligo name	Sequence
3' adapter	5'-rAppNNTGACTGTGGAATTCTCGGGT(fl)GCCAAGG-(fl) (MDX-O-226-29.51-2xAF660, Multiplexdx)
5' adapter	5'(aminolinker)GTTCAGAGTTCTACAGTCCGACGATCrNrNr NrN (MDX-O-264, Multiplexdx)
RT Primer	GCCTTGGCACCCGAGAATTCCA
5' short PCR primer	CTTCAGAGTTCTACAGTCCGACGA
5' long PCR primer	AATGATACGGCGACCACCGAGATCTACACGTTCAGAGTT CTACAGTCCGA
HEK293 Cont C1 3' Index primer RPI29-C5	CAAGCAGAAGACGGCATACGAGATATTCCTCCGTGACTG GAGTTCCTTGGCACCCGAGAATTCCA
HEK293 Cont C2 3' Index primer RPI30-C6	CAAGCAGAAGACGGCATACGAGATGTGTTCCTGTGACTG GAGTTCCTTGGCACCCGAGAATTCCA
HEK293 Cont N1 3' Index primer RPI23-B11	CAAGCAGAAGACGGCATACGAGATAACCTTGGGTGACT GGAGTTCCTTGGCACCCGAGAATTCCA
HEK293 Cont N2 3' Index primer RPI24-B12	CAAGCAGAAGACGGCATACGAGATATTGCGTGGTGACTG GAGTTCCTTGGCACCCGAGAATTCCA
HEK293 Virus C1 3' Index primer RPI31-C7	CAAGCAGAAGACGGCATACGAGATAAGCACTGGTGACT GGAGTTCCTTGGCACCCGAGAATTCCA
HEK293 Virus C2 3' Index primer RPI32-C8	CAAGCAGAAGACGGCATACGAGATCTAGCAAGGTGACT GGAGTTCCTTGGCACCCGAGAATTCCA
HEK293 Virus N1 3' Index primer RPI27-C3	CAAGCAGAAGACGGCATACGAGATGTACTCTCGTGACTG GAGTTCCTTGGCACCCGAGAATTCCA

HEK293 Virus N2 3' Index primer RPI28-C4	CAAGCAGAAGACGGCATACGAGATGTAACGACGTGACTGGAGTTCCTTGGCACCCGAGAATTCCA

792

793 **Virus infection in mice**

794 The H1N1 strain of influenza A/PR8 (Puerto Rico/8/34) was propagated in the allantoic
795 cavities of SPF embryonated chicken eggs for 48-72 hours at 37°C. The resulting allantoic
796 fluids were collected, aliquoted, and stored at -80°C until use. Virus titers were assessed by
797 $TCID_{50}$ assay on MDCK cells as previously reported [78]. To infect the mice, they were
798 anaesthetized with isoflurane, and intranasally inoculated with 2000 TCID50 PR8 in 25 µl
799 sterile PBS/0.1%BSA. Control mice received the same volume of PBS intranasally as a mock
800 infection. After three days of infection, lung tissue samples were collected to isolate single
801 cells using the Lung Dissociation Kit (130-095-927, Miltenyl Biotec, Bergisch Gladbach,
802 Germany) following the manufacturer's protocol. RNA and protein were extracted from the
803 isolated single cells to determine viral mRNA and AGO2 distribution. Specifically, the RNA
804 was extracted using a Quick-RNA Miniprep Kit (ZYMO Research) following the
805 manufacturer's protocol, and the protein was extracted using biochemical fractionation method
806 described above. For ATO treatment, mice were injected intraperitoneally with a daily dose of
807 0.15mg/kg ATO in PBS in a volume of 100ul for 4 days.

808

809 **Data availability**

810 The raw RNA-Seq and PAR-CLIP data described in this paper are accessible through the GEO
811 database (https://www.ncbi.nlm.nih.gov/geo/) under accession no. XXX.

812

813 **Statistical analysis**

814 The data from three individual experiments waere assessed by unpaired t-test or Mann-
815 Whithney U-test (GraphPad Prism Software Inc, San Diego, CA, USA) and presented as mean
816 ± SD (standard deviation). A p-value < 0.05 was considered statistically significant.
817 Cumulative distribution was analyzed using Kolmogorov-Smirnov Test using the R package
818 stats.

819

820 **References**

821 1. Wilson, R.C. & Doudna, J.A. Molecular mechanisms of RNA interference. *Annu Rev*
822 *Biophys* **42**, 217-39 (2013).
823 2. van Rij, R.P. et al. The RNA silencing endonuclease Argonaute 2 mediates specific
824 antiviral immunity in Drosophila melanogaster. *Genes Dev* **20**, 2985-95 (2006).
825 3. Li, W.X. et al. Interferon antagonist proteins of influenza and vaccinia viruses are
826 suppressors of RNA silencing. *Proc Natl Acad Sci U S A* **101**, 1350-5 (2004).
827 4. Li, Y. et al. Induction and suppression of antiviral RNA interference by influenza A
828 virus in mammalian cells. *Nat Microbiol* **2**, 16250 (2016).
829 5. Lopez-Orozco, J. et al. The RNA Interference Effector Protein Argonaute 2 Functions
830 as a Restriction Factor Against SARS-CoV-2. *J Mol Biol*, 168170 (2023).
831 6. Backes, S. et al. The Mammalian response to virus infection is independent of small
832 RNA silencing. *Cell Rep* **8**, 114-25 (2014).
833 7. Seo, G.J. et al. Reciprocal inhibition between intracellular antiviral signaling and the
834 RNAi machinery in mammalian cells. *Cell Host Microbe* **14**, 435-45 (2013).
835 8. Aguado, L.C. et al. microRNA Function Is Limited to Cytokine Control in the Acute
836 Response to Virus Infection. *Cell Host Microbe* **18**, 714-22 (2015).
837 9. Diamond, M.S. & Kanneganti, T.D. Innate immunity: the first line of defense against
838 SARS-CoV-2. *Nat Immunol* **23**, 165-176 (2022).
839 10. Schneider, W.M., Chevillotte, M.D. & Rice, C.M. Interferon-stimulated genes: a
840 complex web of host defenses. *Annu Rev Immunol* **32**, 513-45 (2014).
841 11. Versteeg, G.A. et al. The E3-ligase TRIM family of proteins regulates signaling
842 pathways triggered by innate immune pattern-recognition receptors. *Immunity* **38**, 384-
843 98 (2013).
844 12. Wang, X. et al. Influenza A virus NS1 protein prevents activation of NF-kappaB and
845 induction of alpha/beta interferon. *J Virol* **74**, 11566-73 (2000).
846 13. Evseev, D. & Magor, K.E. Molecular Evolution of the Influenza A Virus Non-structural
847 Protein 1 in Interspecies Transmission and Adaptation. *Front Microbiol* **12**, 693204
848 (2021).
849 14. Hale, B.G., Albrecht, R.A. & García-Sastre, A. Innate immune evasion strategies of
850 influenza viruses. *Future Microbiol* **5**, 23-41 (2010).
851 15. Wang, W. et al. RNA binding by the novel helical domain of the influenza virus NS1
852 protein requires its dimer structure and a small number of specific basic amino acids.
853 *Rna* **5**, 195-205 (1999).
854 16. Gack, M.U. et al. Influenza A virus NS1 targets the ubiquitin ligase TRIM25 to evade
855 recognition by the host viral RNA sensor RIG-I. *Cell Host Microbe* **5**, 439-49 (2009).
856 17. Cecere, G. & Grishok, A. A nuclear perspective on RNAi pathways in metazoans.
857 *Biochim Biophys Acta* **1839**, 223-33 (2014).
858 18. Castel, S.E. & Martienssen, R.A. RNA interference in the nucleus: roles for small
859 RNAs in transcription, epigenetics and beyond. *Nat Rev Genet* **14**, 100-12 (2013).
860 19. La Rocca, G. & Cavalieri, V. Roles of the Core Components of the Mammalian miRISC
861 in Chromatin Biology. *Genes (Basel)* **13**(2022).
862 20. Nowak, I. & Sarshad, A.A. Argonaute Proteins Take Center Stage in Cancers. *Cancers*
863 *(Basel)* **13**(2021).
864 21. Sarshad, A.A. et al. Argonaute-miRNA Complexes Silence Target mRNAs in the
865 Nucleus of Mammalian Stem Cells. *Mol Cell* **71**, 1040-1050.e8 (2018).
866 22. Wang, H. et al. Altering Intracellular Localization of the RNA Interference Factors by
867 Influenza A Virus Non-structural Protein 1. *Front Microbiol* **11**, 590904 (2020).
868 23. Wei, W. et al. A role for small RNAs in DNA double-strand break repair. *Cell* **149**,
869 101-12 (2012).

24. Chu, Y., Yue, X., Younger, S.T., Janowski, B.A. & Corey, D.R. Involvement of argonaute proteins in gene silencing and activation by RNAs complementary to a non-coding transcript at the progesterone receptor promoter. *Nucleic Acids Res* **38**, 7736-48 (2010).
25. Lobo, V. et al. Loss of Lamin A leads to the nuclear translocation of AGO2 and compromised RNA interference. 2023.06.05.543674 (2023).
26. Reus, J.B., Trivino-Soto, G.S., Wu, L.I., Kokott, K. & Lim, E.S. SV40 Large T Antigen Is Not Responsible for the Loss of STING in 293T Cells but Can Inhibit cGAS-STING Interferon Induction. *Viruses* **12**(2020).
27. Kosik, I. et al. Neuraminidase inhibition contributes to influenza A virus neutralization by anti-hemagglutinin stem antibodies. *J Exp Med* **216**, 304-316 (2019).
28. Li, X., Gu, M., Zheng, Q., Gao, R. & Liu, X. Packaging signal of influenza A virus. *Virol J* **18**, 36 (2021).
29. Rouillard, A.D. et al. The harmonizome: a collection of processed datasets gathered to serve and mine knowledge about genes and proteins. *Database (Oxford)* **2016**(2016).
30. Lilyestrom, W., Klein, M.G., Zhang, R., Joachimiak, A. & Chen, X.S. Crystal structure of SV40 large T-antigen bound to p53: interplay between a viral oncoprotein and a cellular tumor suppressor. *Genes Dev* **20**, 2373-82 (2006).
31. Qiao, X. et al. Uncoupling DNA damage from chromatin damage to detoxify doxorubicin. *Proc Natl Acad Sci U S A* **117**, 15182-15192 (2020).
32. Joerger, A.C. & Fersht, A.R. Structural biology of the tumor suppressor p53. *Annu Rev Biochem* **77**, 557-82 (2008).
33. Schirle, N.T. & MacRae, I.J. The crystal structure of human Argonaute2. *Science* **336**, 1037-40 (2012).
34. Pfaff, J. et al. Structural features of Argonaute-GW182 protein interactions. *Proc Natl Acad Sci U S A* **110**, E3770-9 (2013).
35. Gencel-Augusto, J. & Lozano, G. p53 tetramerization: at the center of the dominant-negative effect of mutant p53. *Genes Dev* **34**, 1128-1146 (2020).
36. Tweddle, D.A., Malcolm, A.J., Cole, M., Pearson, A.D. & Lunec, J. p53 cellular localization and function in neuroblastoma: evidence for defective G(1) arrest despite WAF1 induction in MYCN-amplified cells. *Am J Pathol* **158**, 2067-77 (2001).
37. Chen, S. et al. Arsenic Trioxide Rescues Structural p53 Mutations through a Cryptic Allosteric Site. *Cancer Cell* **39**, 225-239.e8 (2021).
38. Ivashkiv, L.B. & Donlin, L.T. Regulation of type I interferon responses. *Nat Rev Immunol* **14**, 36-49 (2014).
39. Ishikawa, H. & Barber, G.N. The STING pathway and regulation of innate immune signaling in response to DNA pathogens. *Cell Mol Life Sci* **68**, 1157-65 (2011).
40. Piganis, R.A. et al. Suppressor of cytokine signaling (SOCS) 1 inhibits type I interferon (IFN) signaling via the interferon alpha receptor (IFNAR1)-associated tyrosine kinase Tyk2. *J Biol Chem* **286**, 33811-8 (2011).
41. Sermersheim, M. et al. MG53 suppresses interferon-β and inflammation via regulation of ryanodine receptor-mediated intracellular calcium signaling. *Nat Commun* **11**, 3624 (2020).
42. Pauli, E.K. et al. Influenza A virus inhibits type I IFN signaling via NF-kappaB-dependent induction of SOCS-3 expression. *PLoS Pathog* **4**, e1000196 (2008).
43. Anastasakis, D.G. et al. A non-radioactive, improved PAR-CLIP and small RNA cDNA library preparation protocol. *Nucleic Acids Res* **49**, e45 (2021).
44. Hauptmann, J. et al. Biochemical isolation of Argonaute protein complexes by Ago-APP. *Proc Natl Acad Sci U S A* **112**, 11841-5 (2015).

45. Kuleshov, M.V. et al. The COVID-19 Drug and Gene Set Library. *Patterns (N Y)* **1**, 100090 (2020).
46. Chen, E.Y. et al. Enrichr: interactive and collaborative HTML5 gene list enrichment analysis tool. *BMC Bioinformatics* **14**, 128 (2013).
47. Kuleshov, M.V. et al. Enrichr: a comprehensive gene set enrichment analysis web server 2016 update. *Nucleic Acids Res* **44**, W90-7 (2016).
48. Xie, Z. et al. Gene Set Knowledge Discovery with Enrichr. *Curr Protoc* **1**, e90 (2021).
49. Breuer, K. et al. InnateDB: systems biology of innate immunity and beyond--recent updates and continuing curation. *Nucleic Acids Res* **41**, D1228-33 (2013).
50. Karlas, A. et al. Genome-wide RNAi screen identifies human host factors crucial for influenza virus replication. *Nature* **463**, 818-22 (2010).
51. Kedzierski, L. et al. Suppressor of cytokine signaling (SOCS)5 ameliorates influenza infection via inhibition of EGFR signaling. *Elife* **6**(2017).
52. Liu, Q., Chen, X., Novak, M.K., Zhang, S. & Hu, W. Repressing Ago2 mRNA translation by Trim71 maintains pluripotency through inhibiting let-7 microRNAs. *Elife* **10**(2021).
53. Nguyen, D.T.T. et al. The ubiquitin ligase LIN41/TRIM71 targets p53 to antagonize cell death and differentiation pathways during stem cell differentiation. *Cell Death Differ* **24**, 1063-1078 (2017).
54. Robinson, J.T., Thorvaldsdottir, H., Turner, D. & Mesirov, J.P. igv.js: an embeddable JavaScript implementation of the Integrative Genomics Viewer (IGV). *Bioinformatics* **39**(2023).
55. Iwasaki, A. & Pillai, P.S. Innate immunity to influenza virus infection. *Nat Rev Immunol* **14**, 315-28 (2014).
56. Ji, Z.X., Wang, X.Q. & Liu, X.F. NS1: A Key Protein in the "Game" Between Influenza A Virus and Host in Innate Immunity. *Front Cell Infect Microbiol* **11**, 670177 (2021).
57. Wang, S. et al. AGO2 Negatively Regulates Type I Interferon Signaling Pathway by Competition Binding IRF3 with CBP/p300. *Front Cell Infect Microbiol* **7**, 195 (2017).
58. Rentschler, M. et al. Nuclear Translocation of Argonaute 2 in Cytokine-Induced Senescence. *Cell Physiol Biochem* **51**, 1103-1118 (2018).
59. Lee, S. et al. Virus-induced senescence is a driver and therapeutic target in COVID-19. *Nature* **599**, 283-289 (2021).
60. Tonnessen-Murray, C.A., Lozano, G. & Jackson, J.G. The Regulation of Cellular Functions by the p53 Protein: Cellular Senescence. *Cold Spring Harb Perspect Med* **7**(2017).
61. Krell, J. et al. TP53 regulates miRNA association with AGO2 to remodel the miRNA-mRNA interaction network. *Genome Res* **26**, 331-41 (2016).
62. He, F. et al. Interaction between p53 N terminus and core domain regulates specific and nonspecific DNA binding. *Proc Natl Acad Sci U S A* **116**, 8859-8868 (2019).
63. tenOever, B.R. Questioning antiviral RNAi in mammals. *Nat Microbiol* **2**, 17052 (2017).
64. Cullen, B.R., Cherry, S. & tenOever, B.R. Is RNA interference a physiologically relevant innate antiviral immune response in mammals? *Cell Host Microbe* **14**, 374-8 (2013).
65. Mousavi, S.R. et al. Dysregulation of RNA interference components in COVID-19 patients. *BMC Res Notes* **14**, 401 (2021).
66. Adiliaghdam, F. et al. A Requirement for Argonaute 4 in Mammalian Antiviral Defense. *Cell Rep* **30**, 1690-1701.e4 (2020).

967 67. Ramos, I. et al. Innate Immune Response to Influenza Virus at Single-Cell Resolution
968 in Human Epithelial Cells Revealed Paracrine Induction of Interferon Lambda 1. *J*
969 *Virol* **93**(2019).
970 68. Wang, B. et al. Influenza A Virus Facilitates Its Infectivity by Activating p53 to Inhibit
971 the Expression of Interferon-Induced Transmembrane Proteins. *Front Immunol* **9**, 1193
972 (2018).
973 69. Girardi, E. et al. Cross-species comparative analysis of Dicer proteins during Sindbis
974 virus infection. *Sci Rep* **5**, 10693 (2015).
975 70. Piette, J., Neel, H. & Maréchal, V. Mdm2: keeping p53 under control. *Oncogene* **15**,
976 1001-10 (1997).
977 71. Whitworth, I.T. et al. Defining distinct RNA-protein interactomes of SARS-CoV-2
978 genomic and subgenomic RNAs. 2023.05.15.540806 (2023).
979 72. Jumper, J. et al. Highly accurate protein structure prediction with AlphaFold. *Nature*
980 **596**, 583-589 (2021).
981 73. Ewels, P.A. et al. The nf-core framework for community-curated bioinformatics
982 pipelines. *Nat Biotechnol* **38**, 276-278 (2020).
983 74. Love, M.I., Huber, W. & Anders, S. Moderated estimation of fold change and
984 dispersion for RNA-seq data with DESeq2. *Genome Biol* **15**, 550 (2014).
985 75. Wang, L., Wang, S. & Li, W. RSeQC: quality control of RNA-seq experiments.
986 *Bioinformatics* **28**, 2184-5 (2012).
987 76. Martin, M. Cutadapt removes adapter sequences from high-throughput sequencing
988 reads. *2011* **17**, 3 %J EMBnet.journal (2011).
989 77. Corcoran, D.L. et al. PARalyzer: definition of RNA binding sites from PAR-CLIP
990 short-read sequence data. *Genome Biol* **12**, R79 (2011).
991 78. Baer, A. & Kehn-Hall, K. Viral concentration determination through plaque assays:
992 using traditional and novel overlay systems. *J Vis Exp*, e52065 (2014).

993
994

995 **FIGURES**

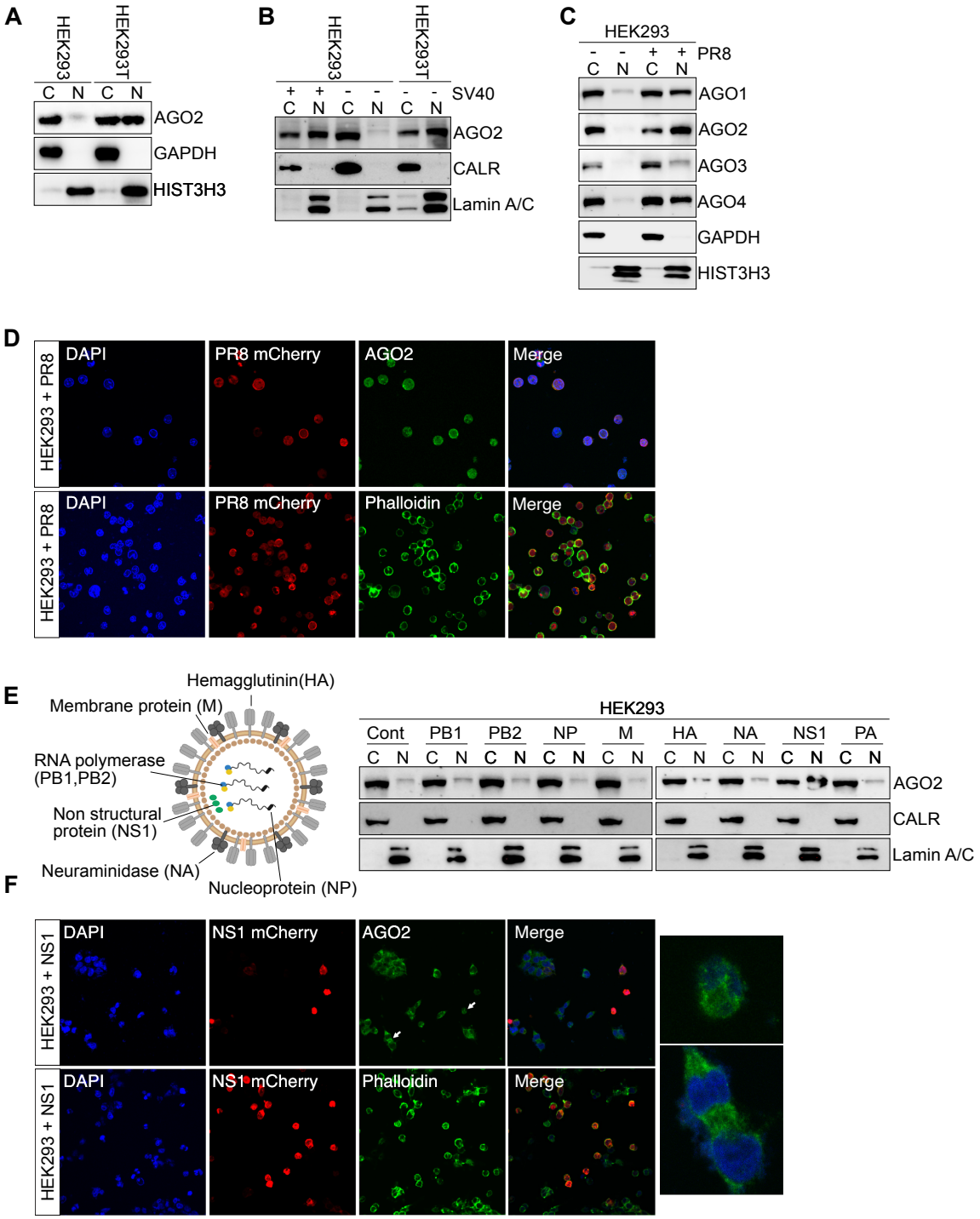

996
997 **Figure 1 – IAV virus NS1 induces AGO2 nuclear translocation**

998 **(A)** Representative AGO2 immunoblots from cytoplasmic (C) and nuclear (N) lysates in
999 HEK293 and HEK293T cells. GAPDH served as cytoplasmic marker and HIST3H3 as nuclear
1000 marker. n=3

1001 **(B)** Representative AGO2 immunoblots from cytoplasmic (C) and nuclear (N) lysates in
1002 HEK293 cells transfected with plasmid expressing SV40 Large T antigen. HEK293T was used

1003 as a positive control. CALR served as cytoplasmic marker and Lamin A/C as nuclear marker.
1004 n=3

1005 **(C)** Representative AGO1, AGO2, AGO3 and AGO4 immunoblots from cytoplasmic (C) and
1006 nuclear (N) lysates in HEK293 cells infected with PR8 virus at MOI 10 for 16 hours. GAPDH
1007 served as cytoplasmic marker and HIST3H3 as nuclear marker. n=3

1008 **(D)** Immunofluorescence images of AGO2 and PR8-mCherry in HEK293 infected with PR8-
1009 NS1-mCherry virus at MOI 10 for 16 hours. Phalloidin and DAPI stained for F-actin and DNA,
1010 respectively. n=3

1011 **(E)** Representative AGO2 immunoblots from cytoplasmic (C) and nuclear (N) lysates in
1012 HEK293 cells transfected with PB1, PB2, NP, M, HA, NS1, and PA expressing plasmids for
1013 2 days. CALR served as cytoplasmic marker and Lamin A/C as nuclear marker. n=3

1014 **(F)** Immunofluorescence images of AGO2 and NS1-mCherry in HEK293 infected with NS1-
1015 mCherry virus at MOI 10 for 16 hours. Phalloidin and DAPI stained for F-actin and DNA,
1016 respectively. n=3

1017

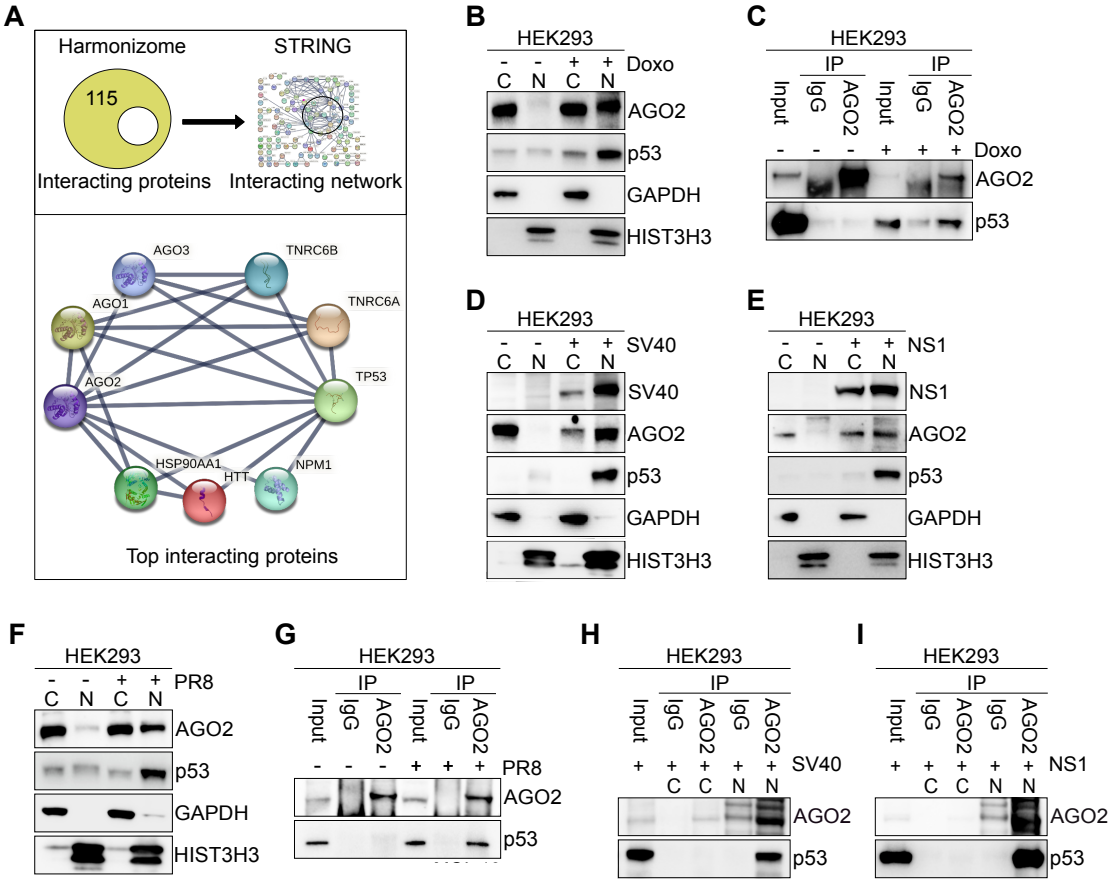

Figure 2 – p53 associates with AGO2 in the nucleus

(A) STRING protein-protein interaction network of AGO2.

(B) Representative AGO2 and p53 immunoblots from cytoplasmic (C) and nuclear (N) lysates in HEK293 cells treated with Doxorubicin (Doxo) for 24 hours. GAPDH served as a cytoplasmic marker and HIST3H3 served as nuclear marker. n=3

(C) AGO2 immunoprecipitation (IP) from HEK293 cells treated with Doxorubicin (Doxo) for 24 hours. Representative immunoblots of AGO2 and p53. n=3

(D) Representative AGO2, p53 and SV40 immunoblots from cytoplasmic (C) and nuclear (N) lysates in HEK293 cells transfected with SV40 large T antigen expressing plasmid. GAPDH served as a cytoplasmic marker and HIST3H3 served as nuclear marker. n=3

(E) same as in **(D)** except for immunoblots for NS1 in HEK293 cells transfected with NS1 mCherry expressing plasmid for 24 hours. n=3

(F) Representative AGO2 and p53 immunoblots from cytoplasmic (C) and nuclear (N) lysates in HEK293 cells infected with PR8 virus at MOI 10 for 16 hours. GAPDH served as cytoplasmic marker and HIST3H3 as nuclear marker. n=3

(G) AGO2 immunoprecipitation (IP) from HEK293 cells treated with PR8 virus at MOI 10 for 16 hours. Representative immunoblots of AGO2 and p53. n=3

1036 **(H)** AGO2 immunoprecipitation (IP) from cytoplasmic and nuclear fractions in HEK293 cells
1037 transfected with SV40 large T antigen expressing plasmid for 24 hours. Representative
1038 immunoblots of AGO2 and p53. n=3

1039 **(I)** same as in **(H)** except for HEK293 cells were transfected with NS1 expressing plasmid for
1040 24 hours. n=3

1041

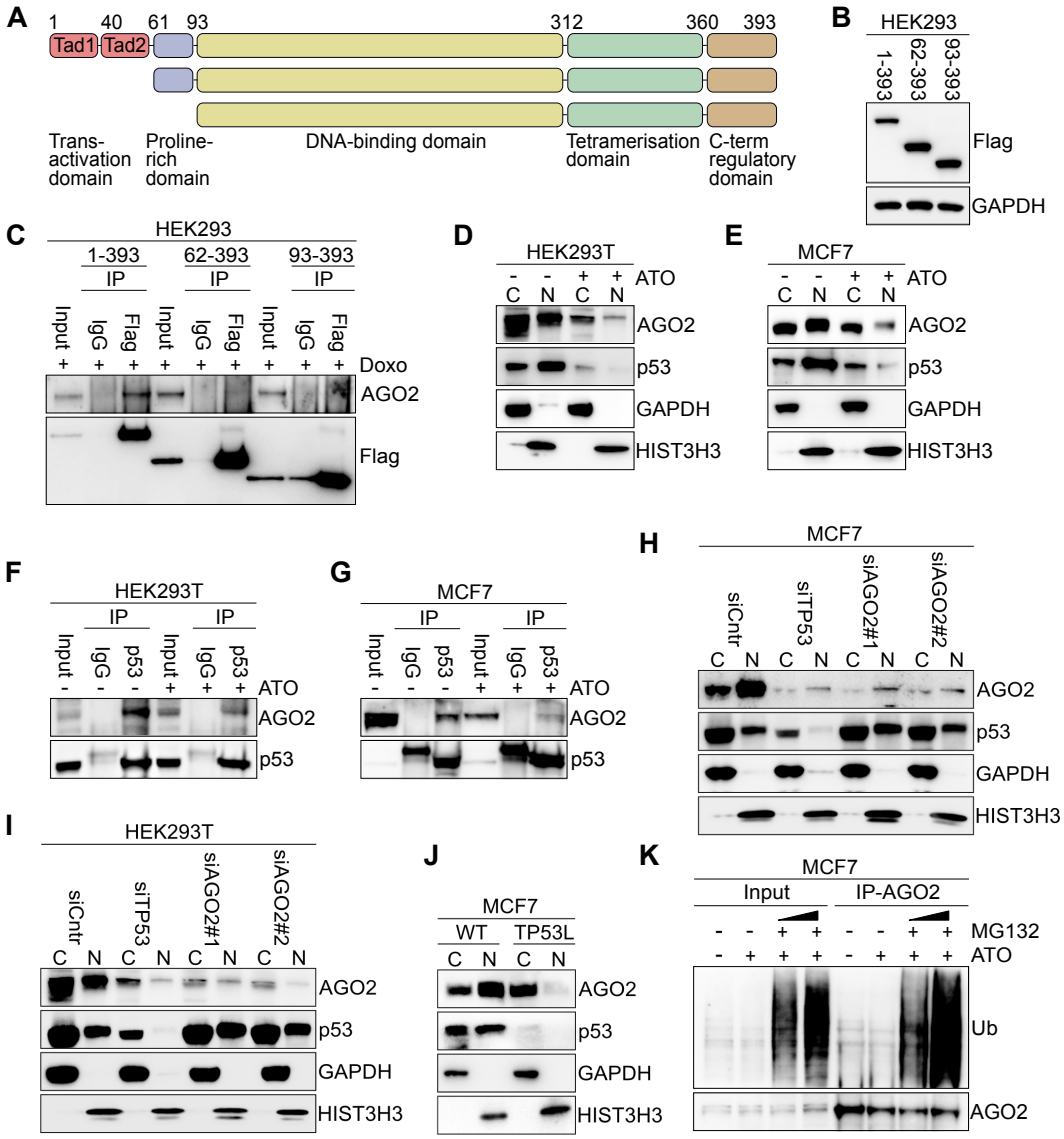

Figure 3 – Tetrameric p53 protects nuclear AGO2 from proteasomal degradation

(A) Schematic diagram of human p53 protein and N-terminal truncated Flag-tagged p53 isoforms used in the study.

(B) Representative Flag immunoblots from HEK293 cells transfected with Flag-WT-p53 or N-terminally Flag-tagged p53 mutants. GAPDH served as a loading control. n=3

(C) Flag immunoprecipitation (IP) from HEK293 cells transfected with plasmids expressing Flag-WT-p53 or N-terminally Flag-tagged p53 mutant. HEK293 cells were transfected with the p53 plasmids for 1 day and then treated with 1 µg/mL Doxorubicin (Doxo) for 1 more day. Representative immunoblots of AGO2 and Flag are indicated. n=3

(D) Representative AGO2 and p53 immunoblots from cytoplasmic (C) and nuclear (N) lysates in HEK293T cells treated with 0.5 µg/mL arsenic trioxide (ATO) for 24 hours. GAPDH served as a cytoplasmic marker and HIST3H3 served as nuclear marker. n=3

1055 **(E)** Same as in **(D)** but in MCF7 cells. n=3

1056 **(F)** p53 immunoprecipitation (IP) from HEK293T cells treated with 0.5 μg/mL Arsenite
1057 trioxide (ATO) for 24 hours. Representative immunoblots of AGO2 and p53. n=3

1058 **(G)** same as in **(F)** but in MCF7 cells. n=3

1059 **(H)** Representative AGO2 and p53 immunoblots from cytoplasmic (C) and nuclear (N) lysates
1060 in MCF7 cells treated with siRNAs for 24 hours. siCntr: control scramble siRNAs; siTP53:
1061 siRNA specific for TP53; and siAGO2: two different siRNAs specific for AGO2. GAPDH
1062 served as a cytoplasmic marker and HIST3H3 served as nuclear marker. n=3

1063 **(I)** Same as in **(H)** but in HEK293T cells. n=3

1064 **(J)** Representative AGO2 and p53 immunoblots from cytoplasmic (C) and nuclear (N) lysates
1065 in WT MCF7 cells or TP53L MCF7 cells. GAPDH served as a cytoplasmic marker and
1066 HIST3H3 served as nuclear marker. n=3

1067 **(K)** AGO2 immunoprecipitation (IP) from MCF7 cells treated with 2 μg/ml MG132 for 2 hours
1068 before additional 24 hours of treatment with 0.5 μg/ml arsenic trioxide (ATO). Representative
1069 immunoblots of ubiquitin (Ub) and AGO2. n=3

1070
1071

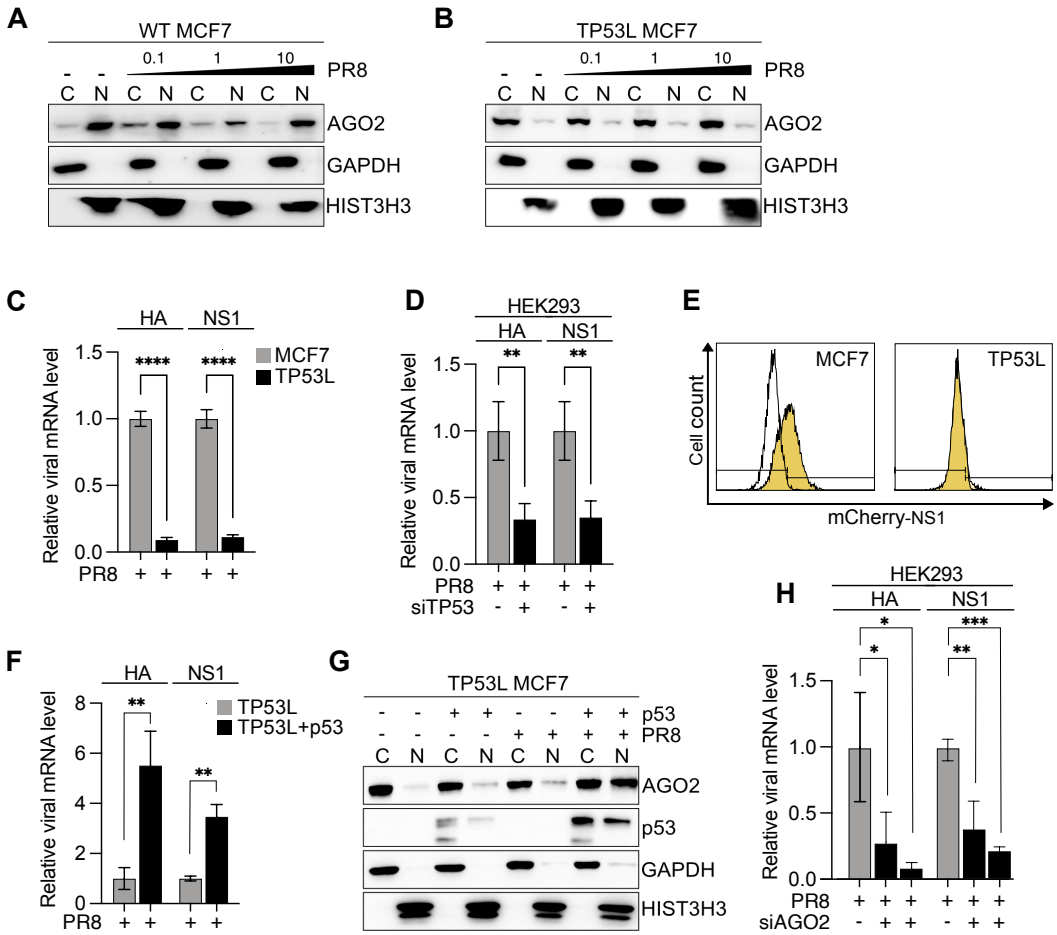

Figure 4 – Nuclear AGO2 supports viral replication

(A) Representative AGO2 immunoblots from cytoplasmic (C) and nuclear (N) lysates in WT MCF7 cells infected with PR8 virus at MOI 0.1; 1; 10 for 16 hours. GAPDH served as a cytoplasmic marker and HIST3H3 served as nuclear marker. n=3

(B) Same as in **(A)** but in TP53L MCF7 cells. n=3

(C) Relative expression, as measured by RT-qPCR, of NS1 and HA mRNA levels in WT MCF7 cells and TP53L MCF7 cells upon infection with PR8 virus at MOI 10 for 16 hours. GAPDH was used as a reference gene. Bars are mean and error bars represent ± SD. **** $p<0.0001$ by unpaired t-test. n=3

(D) RT-qPCR of NS1 and HA mRNA levels in HEK293 cells treated with siRNAs against TP53 (siTP53) for 48 hours. 16 hours before the end of incubation, cells were infected with PR8 virus at MOI 10. GAPDH was used as a reference gene. Bars are mean and error bars represent ± SD. **** $p<0.0001$ by unpaired t-test. n=3

(E) Flow cytometry analysis of NS1-mCherry protein expression in WT MCF7 cells and TP53L MCF7 cells upon infection with PR8 virus at MOI 10 for 16 hours. White histogram shows mock-infected cells while yellow histogram is PR8-infected. n=3

(F) Relative expression, as measured by RT-qPCR, of NS1 and HA mRNA levels in WT MCF7 and TP53L MCF7 cells. TP53L MCF7 cells were transfected with Flag-WT-p53 expressing

1091 plasmids for 24 hours. Subsequently, both WT MCF7 cells and TP53L MCF7 overexpressing
1092 WT p53 transiently were infected with PR8 virus at MOI 10 for 16 additional hours. GAPDH
1093 was used as a reference gene. Bars are mean and error bars represent ± SD. ** $p<0.01$ by
1094 unpaired t-test. n=3

1095 **(G)** Representative AGO2 and p53 immunoblots from cytoplasmic (C) and nuclear (N) lysates
1096 in TP53L MCF7 cells transfected with Flag-WT-p53 expressing plasmids for 24 hours and
1097 infected with PR8 virus at MOI 10 for 16 additional hours**.** GAPDH served as a cytoplasmic
1098 marker and HIST3H3 served as nuclear marker. n=3

1099 **(H)** Relative expression, as measured by RT-qPCR, of NS1 and HA mRNA levels in HEK293
1100 cells treated with two different siRNAs against AGO2 (siAGO2) for 48 hours. 16 hours before
1101 the end of incubation, cells were infected with PR8 virus at MOI 10. GAPDH was used as a
1102 reference gene. Bars are mean and error bars represent ± SD. * $p<0.05$, ** $p<0.01$, *** $p<0.001$
1103 by unpaired t-test. n=3

1104

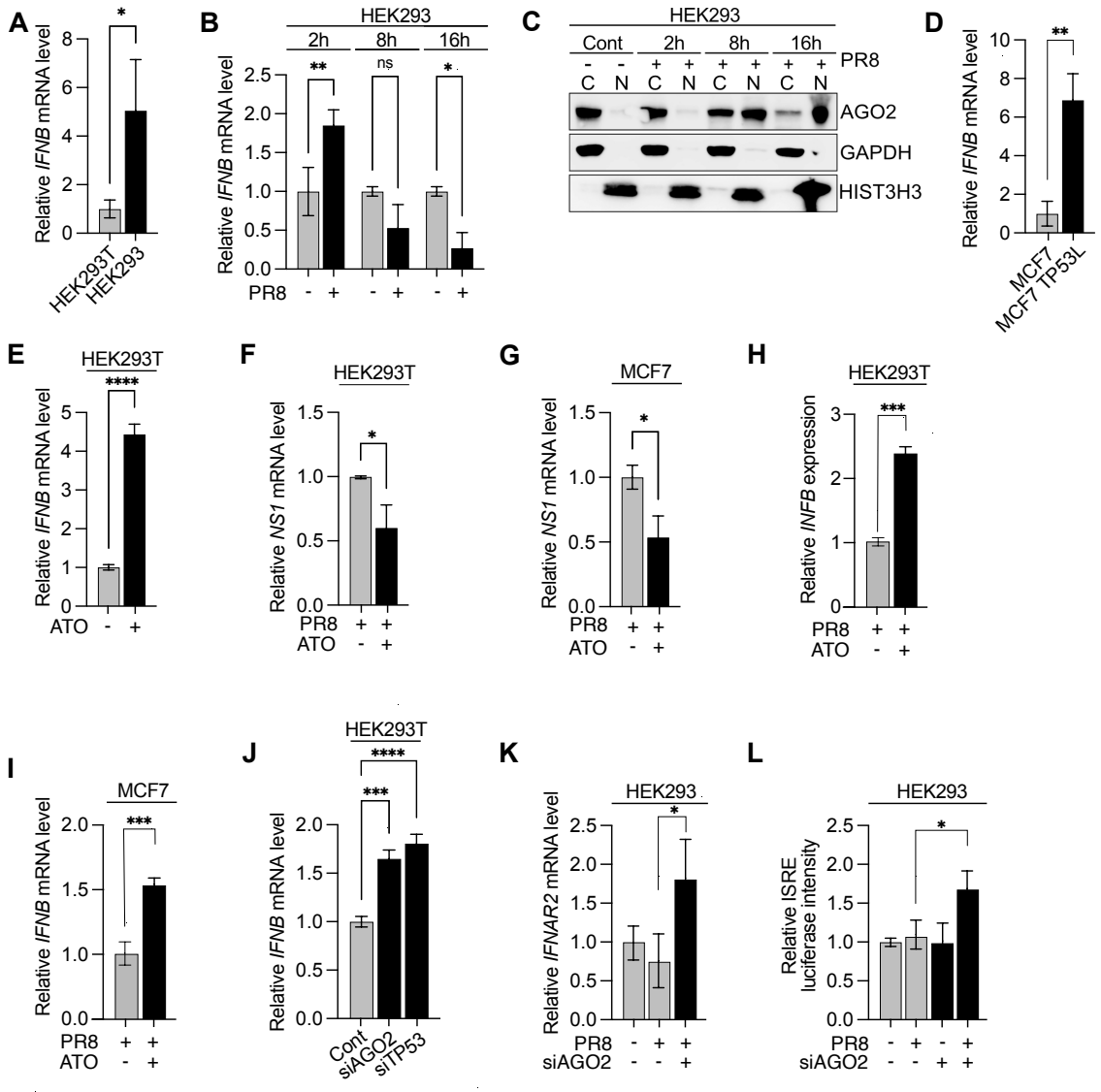

Figure 5 – Nuclear AGO2 downregulates *IFNB* and other type-I-IFN related genes

(A) Relative expression, as measured by RT-qPCR, of IFNB mRNA levels in HEK293T and HEK293 cells. GAPDH was used as a reference gene. Bars are mean and error bars represent ± SD. * $p<0.1$ by unpaired t-test. n=3

(B) Relative expression, as measured by RT-qPCR, of IFNB mRNA levels in HEK293 cells infected with PR8 virus at MOI 10 for 2, 8 or 16 hours. GAPDH was used as a reference gene. Bars are mean and error bars represent ± SD. * $p<0.05$, ** $p<0.01$ by unpaired t-test. n=3

(C) Representative AGO2 immunoblots from cytoplasmic (C) and nuclear (N) lysates in HEK293 cells infected with PR8 virus at MOI 10 for 2, 8 or 16 hours. GAPDH served as a cytoplasmic marker and HIST3H3 served as nuclear marker. n=3

(D) Relative expression, as measured by RT-qPCR, of IFNB mRNA levels in WT MCF7 cells and TP53L MCF7 cells. GAPDH was used as a reference gene. Bars are mean and error bars represent ± SD. ** $p<0.01$ by unpaired t-test. n=3

1119 **(E)** Relative expression, as measured by RT-qPCR, of IFNB mRNA levels in HEK293T cells
1120 treated for 24 hours with 0.5 μg/ml arsenic trioxide (ATO). GAPDH was used as a reference
1121 gene. Bars are mean and error bars represent ± SD. **** $p<0.0001$ by unpaired t-test. n=3

1122 **(F)** Relative expression, as measured by RT-qPCR, of NS1 mRNA levels in HEK293T cells
1123 treated for 24 hours with 0.5 μg/ml arsenic trioxide (ATO) or vehicle and infected with PR8
1124 virus at MOI 10 for 16 hours. GAPDH was used as a reference gene. Bars are mean and error
1125 bars represent ± SD. * $p<0.05$ by unpaired t-test. n=3

1126 **(G)** Relative expression, as measured by RT-qPCR, of IFNB mRNA levels in HEK293T cells
1127 treated for 24 hours with 0.5 μg/ml arsenic trioxide (ATO) or vehicle and infected with PR8
1128 virus at MOI 10 for 16 hours. GAPDH was used as a reference gene. Bars are mean and error
1129 bars represent ± SD. **** $p<0.0001$ by unpaired t-test. n=3

1130 **(H)** same as in **(F)** but in MCF7 cells. n=3

1131 **(I)** same as in **(G)** but in MCF7 cells. n=3

1132 **(J)** Relative expression, as measured by RT-qPCR, of IFNB mRNA levels in HEK293T cells
1133 treated with siRNAs against TP53 or AGO2 for 48 hours. GAPDH was used as a reference
1134 gene. Bars are mean and error bars represent ± SD. *** $p<0.001$, **** $p<0.0001$ by unpaired t-
1135 test. n=3

1136 **(K)** Relative expression, as measured by RT-qPCR, of IFNAR2 mRNA levels in HEK293 cells
1137 treated with siRNA against AGO2 for 48 hours. 16 hours before the end of incubation, cells
1138 were infected with PR8 virus at MOI 10. GAPDH was used as a reference gene. Bars are mean
1139 and error bars represent ± SD. * $p<0.05$ by unpaired t-test. n=3

1140 **(L)** Normalized lucifersase signal of ISRE-transfected HEK293 cells, treated with siRNA
1141 against AGO2 for 48 hours. 16 hours before the end of incubation, cells were infected with
1142 PR8 virus at MOI 10. GAPDH was used as a reference gene. Bars are mean and error bars
1143 represent ± SD. * $p<0.05$ by unpaired t-test. n=3

1144

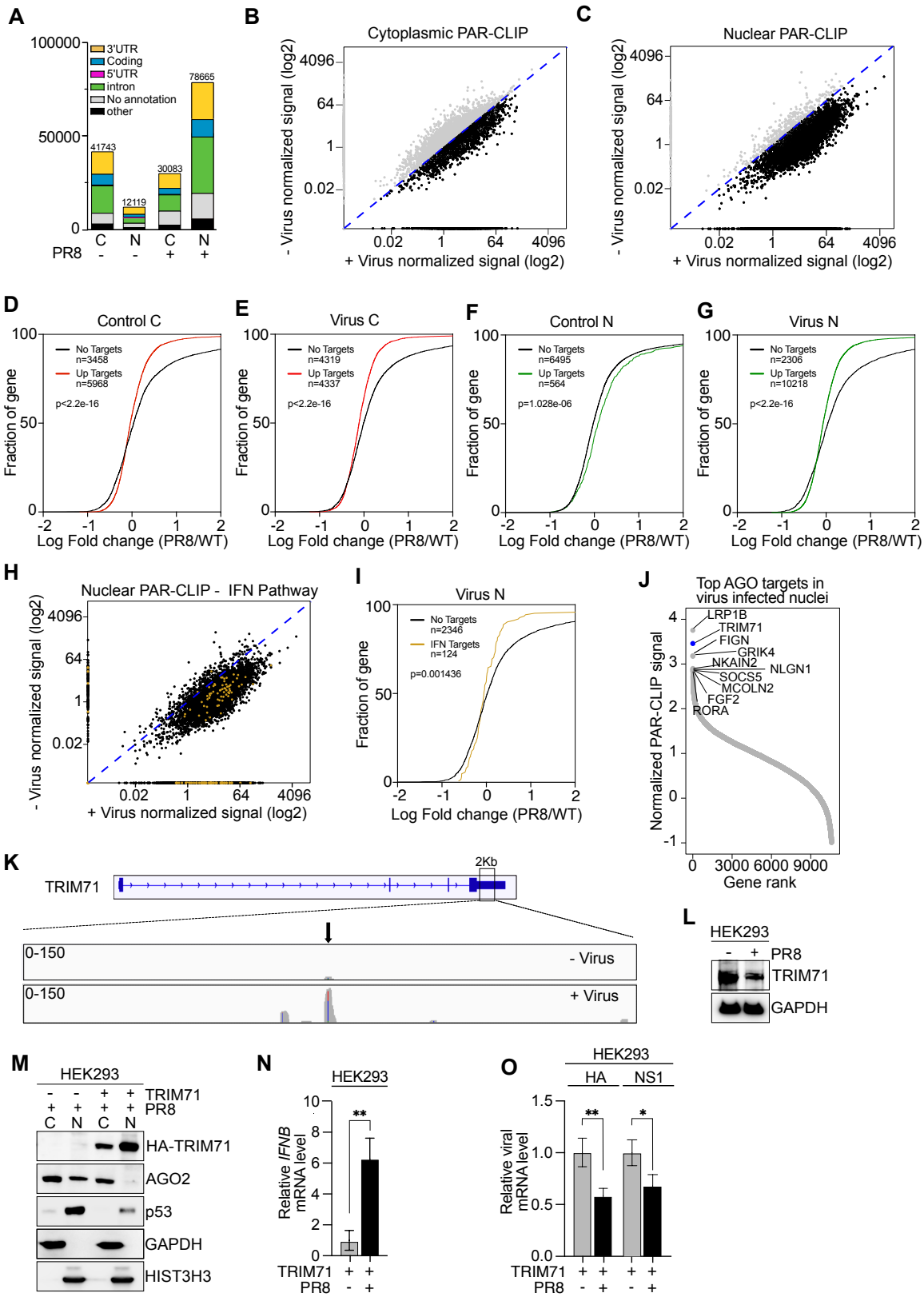

Figure 6 – Nuclear AGO2 downregulates type-I IFN pathway genes and TRIM71 in IAV-infected cells

(A) Distribution of fPAR-CLIP sequence reads in clusters across target RNA across 3′UTR, coding sequence, 5′UTR, and introns from cytoplasmic (C) and nuclear (N) fractions of

1150 HEK293 cells infected with PR8 virus at MOI 10 for 16 hours. The graph shows the average
1151 of 2 independent experiments.

1152 **(B)** Scatter plot of cytoplasmic fPAR-CLIP log2 normalized signal in control (- Virus) and
1153 IAV infected (+Virus) HEK293 cells. Each dots represents a gene and is the average of 2
1154 independent experiments. Blue dashed line shows a perfect correlation. Black dots are genes
1155 with higher PAR-CLIP signal in the IAV-infected sample while grey dots are genes with higher
1156 PAR-CLIP signal in the control sample.

1157 **(C)** same as in **(B)** but for nuclear fPAR-CLIP.

1158 **(D)** Cumulative distribution function of AGO1-4 targets in control cytoplasmic fraction
1159 compared to non-targets. Targets are the genes depicted as grey dots in (**B**)

1160 **(E)** Cumulative distribution function of AGO1-4 targets in virus infected cytoplasmic fraction
1161 compared to non-targets. Targets are the genes depicted as black dots in (**B**)

1162 **(F)** Cumulative distribution function of AGO1-4 targets in control nuclear fraction compared
1163 to non-targets. Targets are the genes depicted as grey dots in (**C**)

1164 **(G)** Cumulative distribution function of AGO1-4 targets in virus infected nuclear fraction
1165 compared to non-targets. Targets are the genes depicted as black dots in (**C**)

1166 **(H)** same graph as in **(C)** but with type-I IFN pathway genes highlighted in golden yellow.

1167 **(I)** same as in **(G)** but for type-I IFN pathway genes.

1168 **(J)** Rank plot showing AGO targets, ordered by normalized PAR-CLIP signal, in IAV infected,
1169 nuclear fraction of HEK293 cells. Each dot represents a gene and is the average of 2
1170 independent experiments.

1171 **(K)** TRIM71 IGV track in nuclear fraction of in control (- Virus) and IAV infected (+Virus)
1172 HEK293 cells.

1173 **(L)** Representative TRIM71 immunoblots from whole cell lysates in HEK293 infected with
1174 PR8 virus at MOI 10 for 16 hours. GAPDH served as a loading control. n= 3

1175 **(M)** Representative HA-TRIM71, AGO2 and p53 immunoblots from cytoplasmic (C) and
1176 nuclear (N) lysates in HEK293 cells transfected with HA-TRIM71 and infected with PR8 virus
1177 at MOI 10 for 16 hours. GAPDH served as a cytoplasmic marker and HIST3H3 served as
1178 nuclear marker. n= 3

1179 **(N)** Relative expression, as measured by RT-qPCR, of IFNB mRNA levels in HEK293 cells
1180 transfected with HA-TRIM71 and infected with PR8 virus at MOI 10 for 16 hours. GAPDH
1181 was used as a reference gene. Bars are mean and error bars represent ± SD. ∗∗ $p<0.01$ by
1182 unpaired t-test. n= 3

1183 **(O)** Relative expression, as measured by RT-qPCR, of HA and NS1 mRNA levels in HEK293
1184 cells transfected with HA-TRIM71 and infected with PR8 virus at MOI 10 for 16 hours.
1185 GAPDH was used as a reference gene. Bars are mean and error bars represent ± SD. ∗ $p<0.05$,
1186 ∗∗ $p<0.01$ by unpaired t-test. n= 3

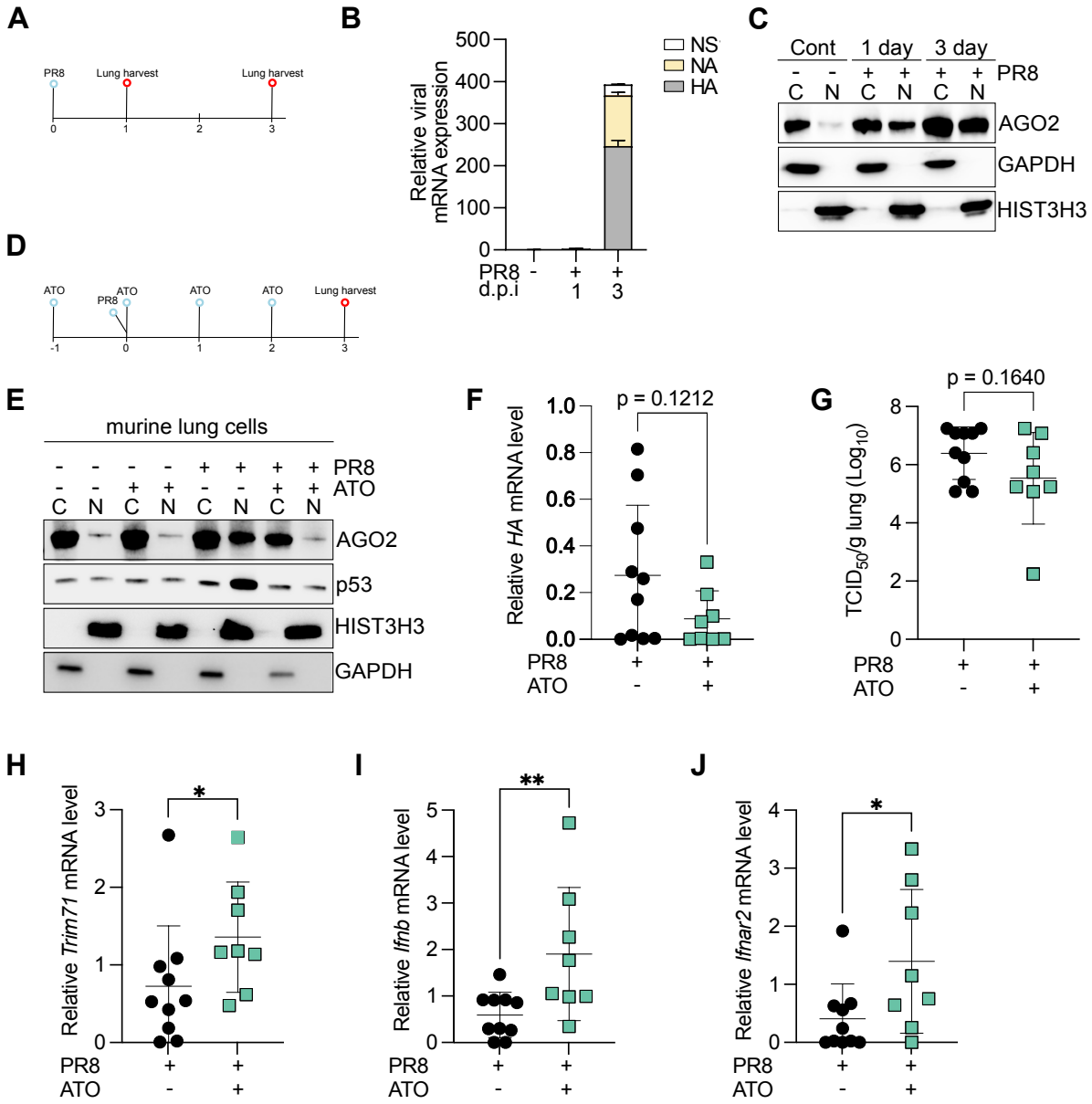

Figure 7 – ATO treatment increases IFN-related genes and decrease viral titers *in vivo.*

(A) Schematic representation of the experimental setup for experiments in **(B)** and **(C)**. Mice were infected i.n. with 2000 $TCID_{50}$ PR8 at day 0 and lungs harvested at 1 and 3 days post-infection.

(B) Relative expression, as measured by RT-qPCR, of NS1 and HA mRNA levels in lung cells isolated from mice at 1 or 3 days post-infection. B-actin was used as a reference gene. Error bars represent ± SD.

(C) Representative AGO2 immunoblots from cytoplasmic (C) and nuclear (N) lysates in lung cells isolated from mice at 1 or 3 days post-infection. GAPDH served as a cytoplasmic marker and HIST3H3 served as nuclear marker. n= 2 independent experiments with 2 mice each

(D) Schematic representation of the experimental setup for experiments in **(E-J)**. Mice were treated daily with i.p. injections of 0.15 mg/kg ATO in PBS (or vehicle), starting from day -1.

1201 At day 0 mice were infected i.n. with 2000 $TCID_{50}$ PR8 and lungs harvested at 3 days post-
1202 infection.

1203 **(E)** Representative AGO2 and p53 immunoblots from cytoplasmic (C) and nuclear (N) lysates
1204 in lung cells isolated from mice treated with ATO and PR8 infected. GAPDH served as a
1205 cytoplasmic marker and HIST3H3 served as nuclear marker. n= 3 independent experiments
1206 with a total of 10 (PR8) and 8 (PR8-ATO) mice.

1207 **(F)** Graph representing HA mRNA levels in lung cells isolated from mice treated treated with
1208 ATO (or vehicle) and PR8 infected. Shown are the individual mice with bar respresenting the
1209 mean and error bars represent ± SD. Statistical analysis was performed by unpaired t-test. n=
1210 3 independent experiments with a total of 10 (PR8) and 8 (PR8-ATO) mice.

1211 **(G)** Graph representing log_{10} $TCID_{50}$/g lung in mice treated treated with ATO (or vehicle) and
1212 PR8 infected. Shown are the individual mice with bar respresenting the mean and error bars
1213 represent ± SD. Statistical analysis was performed by unpaired t-test. n= 3 independent
1214 experiments with a total of 10 (PR8) and 8 (PR8-ATO) mice.

1215 **(H)** Graph representing the mRNA levels of *Trim71* in lung cells isolated from mice treated
1216 treated with ATO (or vehicle) and PR8 infected. Shown are the individual mice with bar
1217 respresenting the mean and error bars represent ± SD. * $p<0.05$ by unpaired t-test. n= 3
1218 independent experiments with a total of 10 (PR8) and 8 (PR8-ATO) mice.

1219 **(I)** same as in **(H)** but for *Ifnb.* ** $p<0.01$ by unpaired t-test.

1220 **(J)** same as in **(H)** but for *Ifnar2.*